Bulletin of the Seismological Society of America, Vol. XX, No. XX, pp. –, – 2018, doi: 10.1785/0120180006

Ⓔ

Ground Motion and Intraevent Variability from 3D Deterministic Broadband (0–7.5 Hz) Simulations along a Nonplanar Strike-Slip Fault

by Kyle B. Withers,[*,†] Kim B. Olsen, Steven M. Day, and Zheqiang Shi[‡]

Abstract We model deterministic broadband (0–7.5 Hz) ground motion from an M_w 7.1 bilateral strike-slip earthquake scenario with dynamic rupture propagation along a rough-fault topography embedded in a medium including small-scale velocity and density perturbations. Spectral accelerations (SAs) at periods 0.2–3 s and Arias intensity durations show a similar distance decay (at the level of 1–2 interevent standard deviations above the median) when compared to Next Generation Attenuation-West2 (NGA)-West2 ground-motion prediction equations (GMPEs) using a $Q(f)$ power-law exponent of 0.6–0.8 above 1 Hz in models with a minimum V_S of 750 m/s. With a trade-off from $Q(f)$, the median ground motion is slightly increased by scattering from statistical models of small-scale heterogeneity with standard deviation (σ) of the perturbations at the lower end of the observed range (5%) but reduced by scattering attenuation at the upper end (10%) when using a realistic 3D background velocity model. The ground-motion variability is strongly affected by the addition of small-scale media heterogeneity, reducing otherwise large values of intraevent standard deviation closer to those of empirical observations. These simulations generally have intraevent standard deviations for SAs lower than the GMPEs for the modeled bandwidth, with an increasing trend with distance (most pronounced in low-to-moderate scattering media) near the level of observations at distances greater than 35 km from the fault. Durations for the models follow the same increasing trend with distance, in which $\sigma \sim 5\%$ produces the best match to GMPE values. We find that a 3D background-velocity model reduces the pulse period into the expected range by breaking up coherent waves from directivity, generating a lognormal distribution of ground-motion residuals. These results indicate that a strongly heterogeneous medium is needed to produce realistic deterministic broadband ground motions. Finally, the addition of a thin surficial layer with low, frequency-independent Q in the model (with a minimum V_S of 750 m/s) controls the high-frequency decay in energy, as measured by the parameter κ, that may be necessary to include as simulations continue to extend to higher frequencies.

Electronic Supplement: Verification of the two-step procedure (converting slip-rate output from dynamic rupture propagation to a kinematic source) by comparing the Support Operator Rupture Dynamics (SORD) and anelastic wave-propagation (AWP) synthetics; misfit of synthetic ground motion modeled with AWP, including small-scale media heterogeneity as compared with frequency–wavenumber ($f-k$), as well as SW4; histograms and q–q plots analyzing the lognormality of ground-motion residuals; figures of ground motion for additional simulations not shown in the main article; and an animation of wave propagation for simulations, including rough-fault topography with and without small-scale media heterogeneity.

Introduction

The strong shaking created by large-magnitude earthquakes is of principal interest to structural engineers to determine the ground motion that buildings and other structures must be able to endure. Typically, a structure's response is

*Now at U.S. Geological Survey, Geologic Hazards Science Center, 1711 Illinois Street, Golden, Colorado 80401.

†Also at Institute of Geophysics and Planetary Physics, 9500 Gilman Drive, University of California, San Diego, La Jolla, California 92093.

‡Now at Tokio Marine Technologies, LLC, 2160 Satellite Boulevard 400, Duluth, Georgia 30097.

designed to withstand a peak value described by some metric, such as peak ground acceleration (PGA) or pseudospectral acceleration (PSA) at a certain frequency. Ground-motion prediction equations (GMPEs) seek to predict the underlying ground motion using empirical observations. Along with a median value, there is also an uncertainty associated with the GMPEs' predictions that can be separated into interevent (between-event) and intraevent (within-event) terms (Atik *et al.*, 2010). The ability to estimate seismic hazard is limited by the finite amount of empirical data from prior earthquakes. For example, at moment magnitudes $> \sim 6$, there is a shortage of observations (e.g., Boore *et al.*, 2015) at distances close to the source ($< \sim 20$ km), and variability is typically modeled to be independent of distance (but may vary as a function of period); thus, characteristics from simulations, if deemed realistic, are useful to supplement the database.

3D wave-propagation simulations of ground motions can play a role in the assessment of seismic hazard and risk through prediction of ground motion for scenario earthquakes (e.g., Olsen *et al.*, 2009; Roten *et al.*, 2011). Additionally, they are useful for the planning of earthquake emergency response and public earthquake preparedness exercises, for physics-based seismic hazard assessment (Graves *et al.*, 2010), as well as for complementing GMPEs in regions of poor sampling, as in Day *et al.* (2008), in which simulated basin responses were used in the Next Generation Attenuation (NGA) project. These approaches have been performed at low frequencies ($< \sim 1$ Hz) for many years, and only recently has there been the computational ability to simulate 3D deterministic high-frequency earthquake ground motion at sufficient distances from the source. The frequency range of engineering interest extends up to at least 10 Hz. It is crucial to extend deterministic ground-motion prediction to higher frequencies to better determine the seismic hazard associated with small structures that typically have a resonance frequency larger than 1 Hz.

Deterministic simulations allow one to generate synthetic ground motion of both historical and hypothetical events and to perform analysis of the resulting ground motion using a user-defined station distribution. Broadband hybrid techniques have been developed that combine low-frequency deterministic ground motion with stochastically generated high-frequency components (e.g., Hartzell *et al.*, 2005; Graves and Pitarka, 2010; Mai *et al.*, 2010). These techniques, however, typically lack deterministic information at higher frequencies that may be important in predicting strong ground motion. A recent push has been made to extend deterministic simulations to higher frequencies, using purely physics-based simulations (Andrews and Ma, 2016; Graves and Pitarka, 2016; Roten *et al.*, 2016; Taborda *et al.*, 2016; Mai *et al.*, 2017). The source and surrounding medium needs to be defined in sufficient detail to model the high-frequency synthetics accurately. This includes ensuring that the source has energy content comparable to observations and implementing complex velocity structure that can be modeled by matching borehole studies in a statistical sense. Additionally, anelastic attenuation (energy losses from absorption into the medium) can dramatically affect the ground motions. Previous studies have been primarily limited to constant-Q across the modeled bandwidth; a more realistic representation of the Earth is to model anelastic attenuation as a varying function of frequency.

This is part 1 of a two-part study that studies broadband ground motion from deterministic simulations employing rough faults in varying complexity media in the subsequent wave propagation. The purpose of this study is to determine if realistic broadband ground motion (characterized by the median and standard deviation, as compared with empirical observations) can be obtained from deterministic modeling and to investigate the effects of anelastic attenuation and scattering at high frequencies (> 1 Hz) with an extended source along a nonplanar strike-slip fault. Part 2 of this work incorporates a similar approach, focused on broadband ground motion from dynamic rupture simulations along a blind-thrust fault, modeled off the geometry of the 1994 M_w 6.7 Northridge earthquake. References to the companion paper are made throughout the article when a finding is contrasted or further enforced with that of the dip-slip events. In both studies, we extend 3D deterministic simulations to higher frequencies using a source that is consistent with that of data, in the sense that ground motion has a roughly flat Fourier amplitude acceleration spectrum, without violating physical constraints on the fault (such as initial stress conditions and fault opening). The high-frequency seismic energy is generated by fault surface roughness, a universally observed feature of natural faults. Here, we model broadband (0–7.5 Hz) ground motion of a generic strike-slip fault with rough-fault topography for distances up to 60 km from the source and compare it with that of recent GMPEs. We include frequency-dependent anelastic attenuation via a power law above a reference frequency (with Q set as a constant below this) and superimpose small-scale heterogeneity on both 1D-layered and 3D Community Velocity Model (CVM) background velocity models. We also estimate the pulse period obtained from our simulations and compare it with that of observations to determine the significance of 3D velocity structure on directivity. Additionally, we examine κ, the decay in high-frequency energy (Anderson and Hough, 1984), as a function of distance, and introduce a shallow constant-Q zone in the near surface that serves to simulate the site-component of κ, referred to as κ_0.

Background

We first briefly summarize the components that we include within our simulations that are usually ignored in low-frequency simulations but that may become necessary when modeling high-frequency ground motion. In addition, we highlight the results of previous work that has studied each of these elements (typically) individually.

Rough-Fault Topography

Faults are observed to have roughness at all scales, ranging from the map scale (such as branching and segmentation; e.g., Ben-Zion and Sammis, 2003) to the finer scale with topographic complexity along the fault-slip surfaces (e.g., Power and Tullis, 1991; Renard *et al.*, 2006). This roughness has been modeled by a self-similar fault surface in deterministic simulations (Dunham *et al.*, 2011) with a single power-law spectral density function. The synthetic ground motions produced from dynamic rupture along a rough-fault surface have been shown to match the characteristics of real data, having a flat power spectrum up to some cutoff frequency (Shi and Day, 2013; Mai *et al.*, 2017). As the earthquake rupture propagates along a nonplanar surface, it creates high-frequency radiation as the rupture front both accelerates (and decelerates). This recent addition of realistic fault topography in 3D simulations of earthquake source models is just one way ground motion can be deterministically generated more realistically at higher frequencies (some alternatives, in which stochastic stress distributions or heterogenous friction law parameters are imposed along a planar fault, are Ripperger *et al.*, 2007; Baumann and Dalguer, 2014; Andrews and Ma, 2016; Graves and Pitarka, 2016).

Frequency-Dependent Attenuation

The earthquake source is not the only source of complexity in the high-frequency ground motion; anelastic attenuation is also necessary for the accurate simulation of seismic wave propagation. At higher frequencies, for which there are more cycles of wavelengths at a certain distance, viscoelasticity has an even greater effect on the ground motion. Most previous studies implemented Q to be constant across a bandwidth; however, observations indicated that anelastic attenuation seems to decrease at higher frequencies, above about 1 Hz or so (e.g., Raoof *et al.*, 1999; Phillips *et al.*, 2013). Recently, Withers *et al.* (2015) implemented this behavior in the form of a power law above a transition frequency (and Q constant below this). They found that a simulation with an exponent of 0.8 above 1 Hz had significantly more energy up to 4 Hz, a trend that increased with distance from the source, compared to a constant-Q model, and better agreed with both strong ground motion records and GMPE relations.

Small-Scale Heterogeneity

Scattering in the Earth's crust caused by small-scale velocity and density heterogeneities in the medium can also affect the seismic ground motion, including amplitudes, travel times, and phase. State-of-the-art CVMs, for example, the Southern California Earthquake Center CVMS and CVM-H, resolve velocity structure at scale lengths on the order of kilometers. However, to be able to resolve the ground motion at frequencies > 1 Hz requires resolution on a much smaller scale. Currently, it is not possible to capture the location-specific small-scale velocity variation in the medium at this scale length over a large region; thus statistical methods are used to depict its variability.

Previous work analyzed the statistical properties of these small-scale variations in well logs and tomography in southern California (Nakata and Beroza, 2015; Savran and Olsen, 2016) and found parameters describing the medium, assuming a Von Karman autocorrelation function. The power spectrum of a distribution describing small-scale heterogeneity, defined by the Fourier transform of the correlation function, depends on the Hurst exponent, determining the spectral decay at high wavenumbers (controlling the roughness of the medium), as well as the correlation length and standard deviation. These studies found a vertical correlation length up to 150 m, a Hurst exponent near 0.0 (indicating that the medium is very rough and rich in short wavelength heterogeneities), and bounds of approximately 5%–10% on the coefficient of variation. Additionally, Shaw *et al.* (2014) and Nakata and Beroza (2015) estimated a horizontal to vertical anisotropic factor of the correlation length in the 5–10 range (i.e., ellipsoidal anisotropy).

Previous studies investigated the impact of small-scale statistical variations of the crust in wave-propagation simulations and on the resulting ground motions (e.g., Frankel and Clayton, 1986; Hartzell *et al.*, 2010; Imperatori and Mai, 2013; Bydlon and Dunham, 2015; Graves and Pitarka, 2016) by imposing a distribution of velocity or density perturbations characterized by various autocovariance functions. For example, Frankel and Clayton (1986) found that small-scale heterogeneities described by a Von Karman autocorrelation function best-explained features seen in seismic records. They found that weak (~5%) standard deviations in random fractal crustal velocity fluctuations are required to explain observed body-wave travel-time variations and high-frequency coda waves. Hartzell *et al.* (2010) looked at the effects of random correlated velocity perturbations on predicted peak horizontal ground velocities and the effect of different correlation lengths and standard deviations for simulations extending up to 1 Hz. They found that there was a significant increase in the variability of ground motion in the entire modeled domain compared to the nonperturbed case. Imperatori and Mai (2013) also looked at the influence of small-scale heterogeneity from several earthquake-source models and found a loss of radiation pattern and directivity breakdown at higher frequencies in elastic models, including small-scale heterogeneities, in agreement with Takemura *et al.* (2009). Imperatori and Mai (2013) also found that coda-wave generation is sensitive to the spectral properties of the medium, particularly the correlation length and Hurst exponent and that scattering from small-scale heterogeneity can increase ground-motion complexity at just a few kilometers away from the source.

Methods

We describe the technique chosen to produce deterministic high-frequency ground motion, as well as the imple-

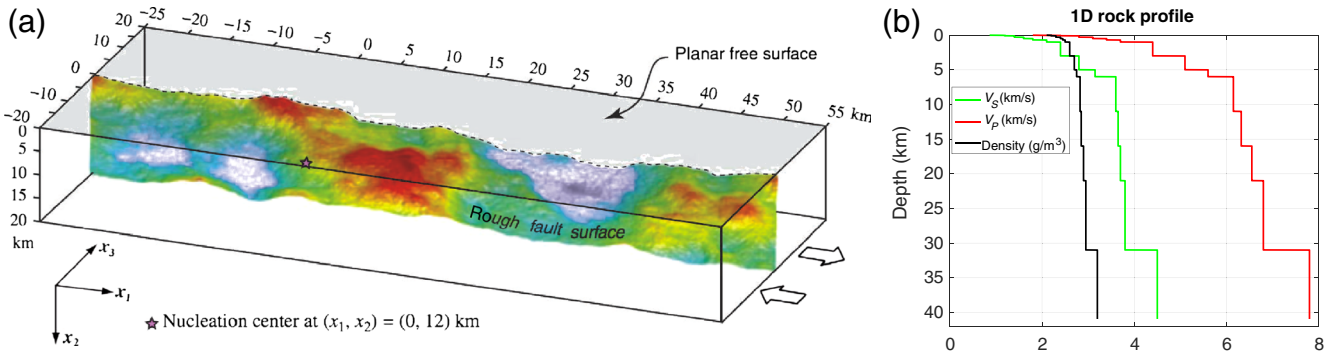

Figure 1. (a) Model geometry and dimensions of the strike-slip rough fault used in this study. The rupture surface uses 4.7 million subfaults that follow a self-similar fractal distribution, with wavelengths ranging from 80 m to 80 km. The strike-slip fault is 80 km in length and 16 km in width. Reproduced in full from Shi and Day (2013). (b) The 1D-layered velocity profile used in the dynamic rupture simulation derived from the Southern California Earthquake Center broadband platform validation exercise for southern California. The color version of this figure is available only in the electronic edition.

mentation of anelasticty and small-scale heterogeneity within the medium.

Source Complexity

We include complexity from a nonplanar fault within our deterministic simulations. A fault roughness model is generated in the wavenumber domain and is designed to follow a self-similar fractal distribution over a specified bandwidth from a vertical mean plane, here more than 3 orders of magnitude (from 80 m to the length of the fault, ~80 km). We use the same fault realization as the dynamic rupture M_w 7.12 scenario, as described by Shi and Day (2013), who studied the effects of fault roughness on rupture propagation and resultant ground motion from a generic right-lateral strike-slip model using the Support Operator Rupture Dynamics (SORD) code (Ely *et al.*, 2009). A strongly rate-weakening friction law was imposed, and the bulk material was subject to Drucker–Prager viscoplasticity, with yielding in shear. Rupture nucleation was achieved by imposing a shear traction perturbation circular patch with a radius of 1 km. The inclusion of Drucker–Prager viscoplasticity allows the off-fault plastic strain to relax what would otherwise be unphysical high-stress concentrations around the rupture tip. The rupture progresses at a generally subshear rupture velocity, and low-confining pressure at shallow depth allows for a small amount of shallow slip. The sampling of the cohesive zone is sufficiently dense throughout the entire model (> 5 grid points) to accurately resolve the slip rate along the fault, which controls the accuracy of the dynamic simulations (Day *et al.*, 2005).

The dynamic rupture simulation performed here incorporates a more realistic medium than the homogenous velocity model in that of Shi and Day (2013). Here, we use a 1D-layered velocity model derived from a characteristic rock site in southern California with a minimum shear-wave velocity of 863 m/s (V_{S30} corresponding to class B of the National Earthquake Hazards Reduction Program boundary site conditions) that rapidly increases with depth. Figure 1 illustrates the fault roughness, depicting a strike-slip model composed of ~5 million subfaults, as well as the velocity model used in the dynamic simulation.

Wave-Propagation Simulation Details

The seismic source in physics-based earthquake simulations can be specified using a kinematic or dynamic representation, in which rupture at each grid point along the fault (subfault) is prescribed *a priori* or evolves spontaneously, respectively. Here, we perform a two-step approach by taking the dynamic rupture slip-rate time histories output from simulation along the rough fault in SORD and convert them to moment-rate time series to input as kinematic sources into anelastic wave propagation (AWP-ODC-GPU), a parallel wave-propagation program (Cui *et al.*, 2013). This finite-difference AWP code is highly scalable, allowing us to extend the ground motions to further distances from the fault and retain high-frequency content. Specifically, the moment-rate tensor elements are $T_{ij} = s\mu A(n_i d_j + n_j d_i)$, in which n and d are unit vectors oriented normal to the fault and along the slip direction, respectively, μ is the shear modulus, and A is the fault surface area associated with the given discretization element (i.e., subfault).

As AWP requires a uniform structured mesh grid, we insert the source directly onto the grid points closest to the rough-fault grid points, with a maximum error of one-half grid spacing in the fault-perpendicular direction. This discretized fault model approximation appears to start to break down at higher frequencies but still retains sufficient accuracy in the bandwidth of interest here (< 7.5 Hz). Verification of the two-step procedure showing SORD and AWP seismograms and frequency spectra comparisons can be found in Ⓔ Figure S1 (available in the electronic supplement to this article) for an elastic half-space. The envelope and phase misfits are less than 5% up to 10 Hz. We deem this as acceptable, because there are inherent differences between the second-order SORD and fourth-order AWP codes that

likely cause larger error than that introduced from the source insertion.

Using this two-step procedure, we assume that anelastic attenuation (not implemented in SORD) along the fault has a negligible effect on the dynamic propagation and that scattering from small-scale heterogeneities in the medium has little effect on the rupture process. The first assumption is supported by Huang *et al.* (2014), who found limited effects on the dynamic rupture propagation from Q, except for large attenuation in damage zones. This second assumption is reasonable, because Bydlon and Dunham (2015) found that variations in slip and rupture velocity are dominantly controlled by fault roughness, and scattering effects only become appreciable beyond about 3 km from the fault.

Medium Complexity

In our simplest models, both the dynamic and kinematic simulations are run in the same laterally homogeneous rock-site profile, as shown in Figure 1. Using a grid spacing of 20 m, we resolve frequencies within the wave propagation within AWP up to a maximum of ~8 Hz (based on an estimated minimum of 5–6 grid points per wavelength at the lowest shear-wave velocity). In addition, we run kinematic simulations in a 3D velocity model extracted from the CVM (Magistrale *et al.*, 2000; Kohler *et al.*, 2003; Lee and Chen, 2014) known as CVM-SI4.26, including a near-surface geotechnical layer (GTL; Ely *et al.*, 2010). Their algorithm uses observed values of V_P, V_S, and ρ in the GTL, replacing information in the upper 350 m with a velocity model derived from V_{S30} maps and interpolated at depth to merge with the background CVM. Taborda and Bielak (2014) analyzed simulations of the 2008 Chino Hills earthquake with and without the GTL and showed that better results are obtained with its inclusion when compared with data. In cases in which we include 3D velocity structure, we clamp the minimum shear-wave velocity to be 863 m/s and then modify V_P, such that the original local V_P/V_S ratio is conserved. In these simulations, we input the fault plane along a 80 km section of the San Andreas fault, located northeast of the Los Angeles basin (see Fig. 2) and rotate our model domain to lie parallel to the mean strike of the fault. The dynamic source (generated in the 1D-layered medium) is inserted in the heterogeneous 3D structure, which modifies the total moment of the simulation (because of the altered shear modulus) by less than 3%.

Our simulations include frequency-dependent attenuation, with constant-Q up to a transition frequency f_T, chosen to be 1 Hz, following a power-law formulation above this threshold:

$$Q(f) = \begin{cases} Q_0 & 0 < f < f_T \\ Q_0 \times (f/f_T)^{\gamma} & f > f_T \end{cases}, \qquad (1)$$

in which Q is the quality factor, Q_0 is the low-frequency value of Q, and $0 \le \gamma \le 1$. For comparison, we also run models with γ of 0, which simply reduces to that of a constant-Q model. We relate the shear-wave velocity to the Q-values: $Q_{S0} = V_S \times C$ and $Q_{P0} = 2 \times Q_S$, in which C is a constant ranging from 0.05 to 0.1 (found to work well in southern California for low-frequency simulations; e.g., Bielak *et al.*, 2010, and references within, and more recently at higher frequencies in Withers *et al.*, 2015) and V_S is the magnitude of shear-wave velocity in m/s.

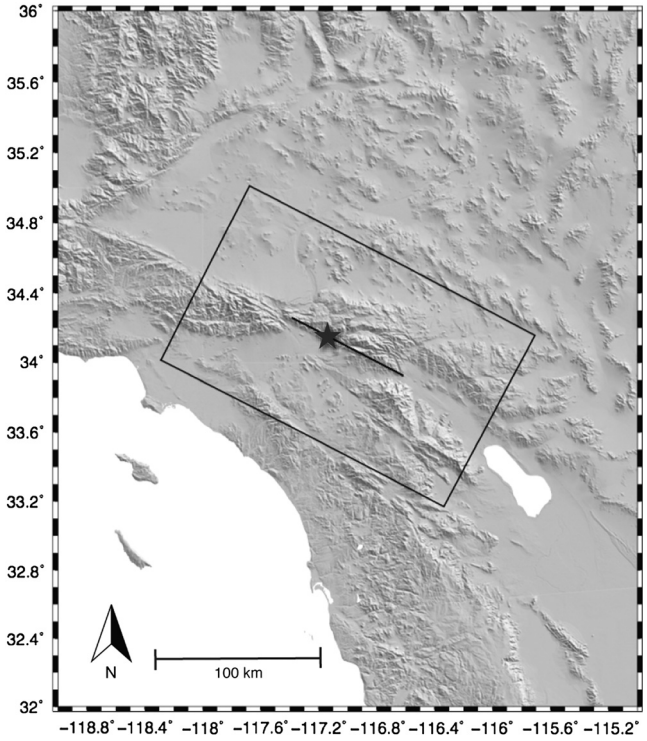

Figure 2. Model domain (rectangle) used to extract the 3D Community Velocity Model (CVM) 4.26i structure with the same dimensions as the 1D-layered simulations (204, 124, and 41 km). The intersection of the fault with the free surface is shown by the line segment, input along an 80 km segment of the San Andreas fault in California. The star depicts the epicenter. Note that free-surface topography is included in the figure to help the reader identify the study region; it is not included in the simulations within this study.

We include small-scale heterogeneity within our models via a Von Karman shape function, which statistically models the variation in the material properties throughout the medium. Heterogeneous 3D velocity models are obtained by superimposing a spatially random field (with zero mean) onto a background deterministic velocity model, as described in Imperatori and Mai (2013). The random perturbations are scaled at each node within the computational grid to maintain the desired (possibly depth dependent) relative standard deviation. We generate a total of six statistical models, with a vertical correlation length ranging from 150 to 1000 m, keeping the Hurst exponent constant at 0.05, a value near that predicted for southern California (Savran and Olsen, 2016). We introduce pattern anisotropy in the model by stretching an isotropic distribution in the horizontal direction by a factor of 5 (as suggested from Nakata and Beroza,

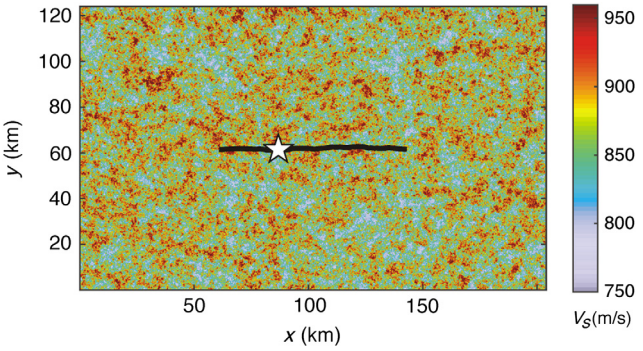

Figure 3. An example of small-scale heterogeneity superimposed on the 1D-layered background model, depicting the variation of V_S(m/s) at the free surface with a correlation length of 150 m, anisotropy factor (vertical-to-horizontal stretch) of 5, $H = 0.05$, and a standard deviation of 5%. The line segment indicates the surface intersection of the rough fault, and the star depicts the epicenter. The color version of this figure is available only in the electronic edition.

2015). The fractal inhomogeneities are incorporated with standard deviations of 5% or 10% (the range estimated by Shaw *et al.*, 2014; Nakata and Beroza, 2015; Savran and Olsen, 2016) for two choices of the random seed.

Figure 3 plots an example from one realization of the shear-wave velocity at the surface after superimposing a statistical fractal model on the 1D-layered velocity profile. To retain accurate simulation of high frequencies, we clamp the shear-wave velocities that extend below 750 m/s in our simulations after superimposing small-scale heterogeneity and keep the original V_P/V_S ratio of the background medium. It is unlikely that this procedure produces a significant bias in overall ground-motion intensity, because only a small percentage ($\ll 1\%$) of the node locations in the medium (and constrained to the surface) are modified with a standard deviation of 5% (with a slightly higher number of node locations at 10%). We apply 3D small-scale heterogeneity throughout the entire medium, even along the fault itself (as opposed to retaining a homogenous region around the source). We will refer to simulations including these statistical variations in velocity and density at short wavelengths in the remainder of the article as models with small-scale heterogeneity.

Figure 4 shows the variation of the shear-wave velocity extracted from CVM-SI4.26 (for the domain outlined in Fig. 2) at 100-m depth, including a GTL as well as a realization of small-scale heterogeneity superimposed onto this 3D background CVM. The longer wavelengths and geologic units formed by fault boundaries and contacts between structural units are largely retained with the addition of statistical variability of random media at shorter wavelengths. The GTL greatly reduces the near-surface velocities; we clamp the background velocity model before adding small-scale heterogeneity to ensure that we do not bias our simulations with only positive variations of heterogeneity. We use 863 m/s as the background minimum shear-wave velocity (again retaining the V_P/V_S ratio of the background model) to match that of our 1D-layered models, which reduces the (lateral) medium complexity in the top 1–2 grid points within our models.

In Figure 5, we qualitatively compare the ground motion without and with small-scale heterogeneity for two snapshots of the fault-parallel component. The figure highlights the complexity originating from both the rough-fault rupture as well as the waves backscattered behind the main arrivals in the model, including small-scale media heterogeneity. An animation of the rough-fault rupture and wave propagation without and with small-scale media heterogeneity is shown in Ⓔ Movie S1.

As seen in Figures 3 and 4, our model domain size is $204 \times 124 \times 41$ km (fault parallel $\times$ fault perpendicular $\times$ vertical), allowing analysis of full azimuthal coverage of R_{rup} (the closest distance to the fault plane) out to 60 km. The ground motion is saved at every fourth grid point (in both horizontal directions) at the surface, equating to a resolution of 80 m. The data points are grouped into distance bins defined by the R_{rup} distance from the mean fault plane (which equals the Joyner–Boore distance R_{JB} for a strike-slip fault), excluding the absorbing boundaries. This results in a minimum of a few thousand stations at each distance interval (at 1 km widths), for a total of just under 4 million stations.

Typically, when working with empirical data, the logarithm of a peak ground-motion parameter or response spectral ordinate is used as a metric to characterize the amplitude of ground motion. Here, we compare GMRotD50 values of PSA at 5% damping (Boore, 2006), as well as the duration (5%–95%) of the Arias intensity. We compute the predicted spectral acceleration (SA) from four NGA-West2 relations (Abrahamson *et al.*, 2014; Campbell and Bozorgnia, 2014; Chiou and Youngs, 2014; Boore *et al.*, 2015) and duration (Afshari and Stewart, 2016) at the same resolution of the output data (we constrain our study to just these four GMPEs for SA because they employ a fairly consistent set of predictor variables, simplifying the analysis). To compute these predictive relations, we use the parameters in the NGA models derived from the fault geometry and background velocity model used in the simulation, including R_{rup}, R_{JB}, $Z_{2.5}$ (the depth to $V_S = 2.5$km/s), V_{S30} (the time-averaged upper 30 m shear-wave velocity), and Z_{tor} (the depth to the top of the rupture).

Results

In this section, we quantify the contribution to the broadband ground motion from frequency-dependent anelastic attenuation and small-scale media heterogeneity in simulations incorporating small-scale fault geometry. We perform an analysis of the synthetic ground-motion median and intraevent variability by comparing against recent GMPEs relations, specifically, SA and duration. We analyze the ground motion simulated from both 1D-layered and 3D CVM background models with and without small-scale medium heterogeneity

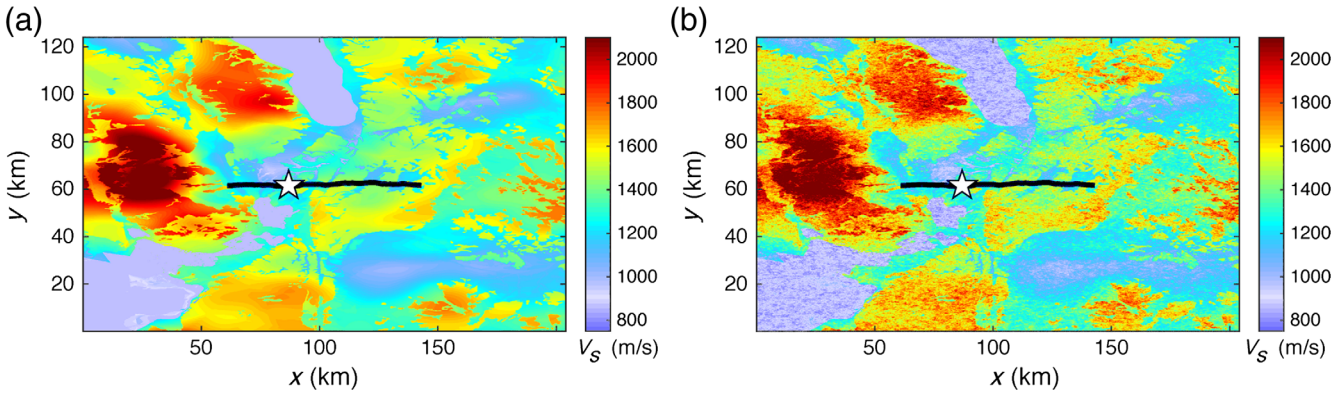

Figure 4. Illustration of media complexity in the near surface (100 m depth). (a) Shear-wave velocity (m/s) extracted from the CVM-SI4.26, including the geotechnical layer. (b) Same as (a) but with the superposition of a statistical model of heterogeneity superimposed on the background 3D model (using the same choice of parameters specified in Fig. 3). The color version of this figure is available only in the electronic edition.

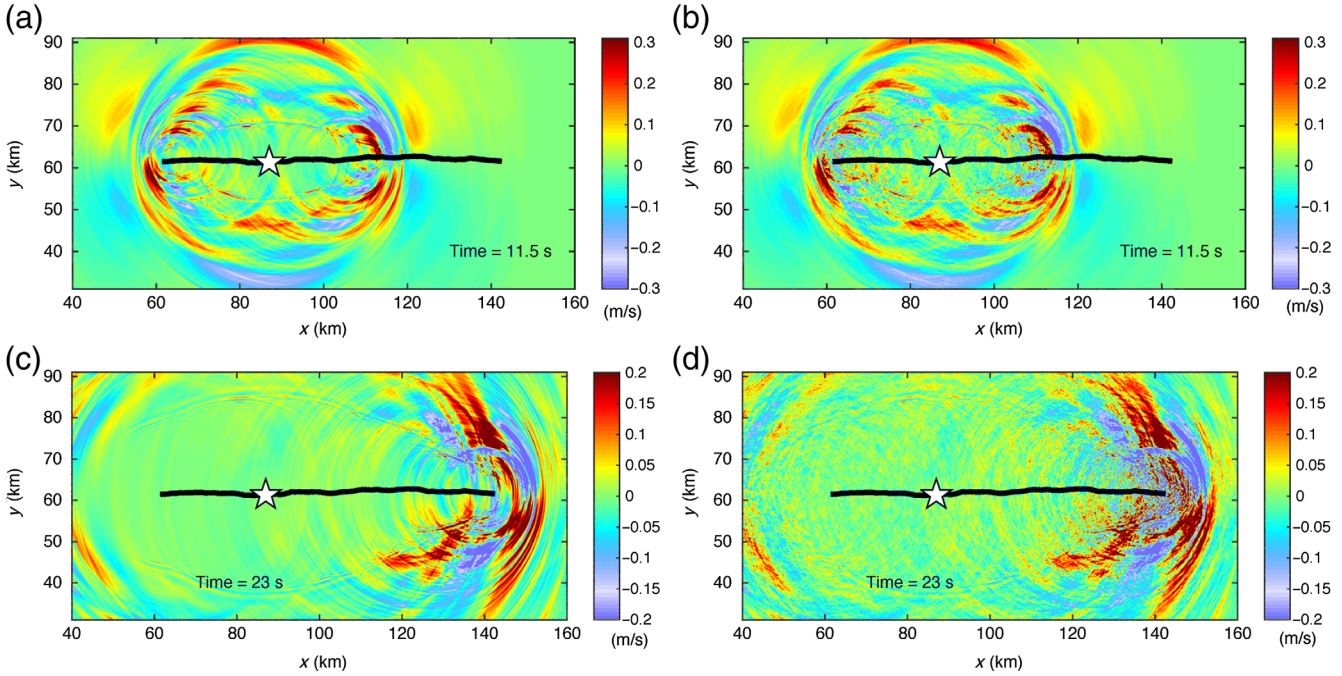

Figure 5. Snapshots of fault-parallel velocity (m/s) at the surface using a 1D-layered model. (a,c) No small-scale media heterogeneity is included. (b,d) Small-scale media heterogeneity included with a vertical correlation length of 150 m, $H = 0.05$, and $\sigma = 5\%$. The color version of this figure is available only in the electronic edition.

for a range of statistical parameters, in combination with different exponents of frequency-dependent attenuation. Additionally, we investigate the effect that medium complexity has on the pulse period, a proxy metric that measures directivity, and compare with that of empirical observations. Finally, we calculate κ from our simulations and introduce a technique to modify the site-effect κ_0 in our simulations.

Anelastic Attenuation

We first isolate the effect on the synthetic ground motion from different anelastic attenuation models using several power-law exponents in equation (1), in addition to varying the constant C that relates Q_0 to V_S. Figure 6 plots the median SA of the synthetic and empirical ground-motion predictions at three periods using the 1D-layered velocity model. Because the different GMPEs use different model parameters and expressions to relate the empirical observations, there is significant variation of the four median GMPE predictions at a specific period, particularly at distances near the fault. We encapsulate this range by shading the full breadth of the four medians (as a function of distance) in Figure 6 and adding the average (of the four GMPE models) ± 1 and $+2$ interevent standard deviations (τ) to the outer

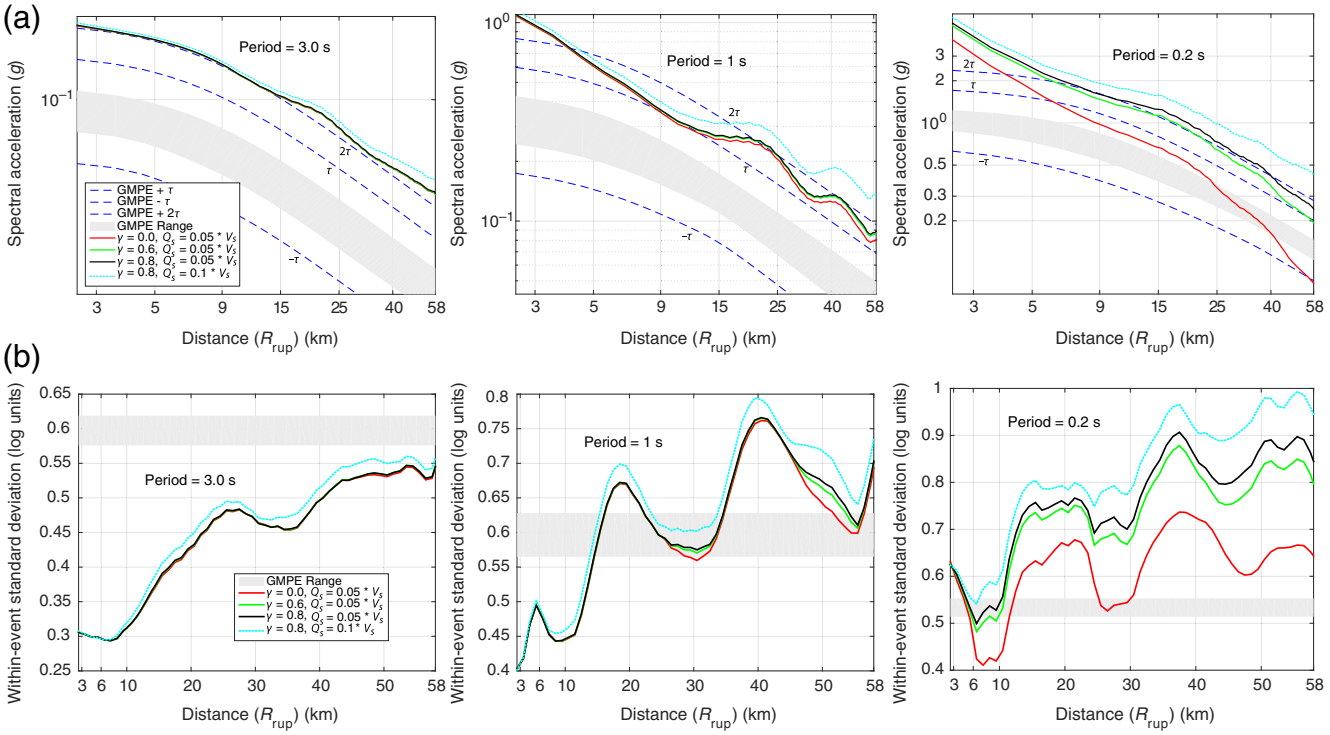

Figure 6. Effect of Q on ground-motion variation for 1D-layered models. (a) The spectral acceleration (SA) median (GMRotD50) for three periods as a function of distance. The shaded region indicates the range of the four ground-motion prediction equation (GMPE) medians, where the dashed lines are the ± 1 and $+2$ interevent standard deviations. Unless specified, $Q_S = 0.05 \times V_S$ and $Q_P = 2 \times V_S$. Binning begins at 2 km from the mean fault plane to avoid the variations in the rough-fault topography at the surface. (b) Intraevent standard deviations as a function of distance, with the shaded area indicating the intraevent standard deviation range of four 2014 GMPE models. Note the linear display in the distance along the abscissa. The color version of this figure is available only in the electronic edition.

bounds of the GMPEs. The corresponding synthetic spatial ground-motion pattern for one choice of attenuation parameters is shown in Figure 7a at a period of 0.3 s.

In general, the synthetic ground-motion decays at the level of 1–2 interevent standard deviations above the median, depending on the period. This larger than average ground motion is mainly due to the source having a high static stress drop, imposed from the initial friction conditions along the fault in the dynamic rupture simulation and thus influencing the magnitude of the final slip distribution (see the Discussion section). As would be expected at a few wavelengths from the source, there are limited differences in anelastic models with a varying $V_S - Q$ relation at longer periods. At higher frequencies, however, anelastic attenuation becomes more important, because there are more wavelengths at an equivalent distance. At short periods, there are differences in the median ground motion even at small R_{rup}; this is due to rupture occurring along a finite fault, where some of the arriving seismic energy has traveled a distance comparable to a sizable fraction of the fault length and thus strongly depend on path effects. It appears that $Q_{S0} = 0.05 \times V_S$ matches the spectral decay consistently well at all periods. Minor differences between models with varying power-law exponents start to appear at periods shorter than 1 s, because SA is sensitive to a finite bandwidth (and thus is influenced by frequencies above 1 Hz). At the shorter period $T = 0.2$, however, it is clear that ground motion attenuates very rapidly in a constant-Q model, deviating increasingly from the GMPE median ground-motion trend as a function of distance. Power-law exponents of 0.6–0.8, with a transition frequency of 1 Hz, better match the decay in energy predicted by the GMPE relations.

Figure 6b plots the intraevent variability, or ϕ, in logarithmic units, calculated from the standard deviations of the residuals (with respect to the mean of the log) at each distance, in addition to the within-event standard deviation range predicted by the four GMPE models. The synthetic variability generally increases as a function of distance at all periods. For example, at long periods ($T = 3$ s), the variability increases almost monotonically from the source to the edge of our model domain, where it is just below the expected level given by GMPE models. At shorter periods (1–0.2 s), the variability oscillates in amplitude as a function of distance, but the overall trend increases at further distances from the fault. When the ground-motion amplitude increases from either adjusting the $V_S - Q$ relation or the power-law exponent, there is greater variability at a particular distance; for example, the constant-Q model ($\gamma = 0.0$) has a lower variability than that of the power-law models at short periods. This stems from the increased deviation of SA from the

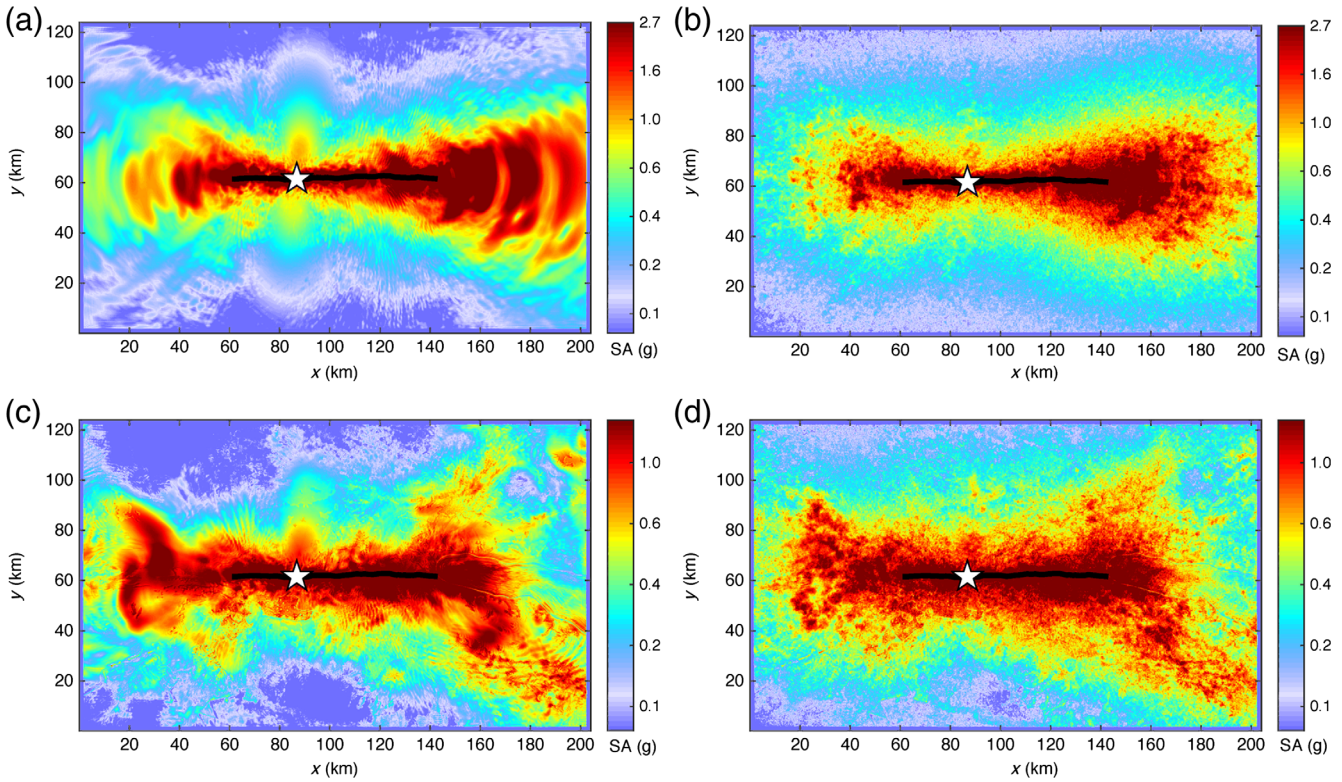

Figure 7. GMRotD50 maps of SA in units of g at $T = 0.3$ s, using various velocity models. (a,c) Models without statistically described media heterogeneity. (b,d) Models with statistically described media heterogeneity using a vertical correlation length of 150 m, $H = 0.05$, and $\sigma = 5\%$. (a,b) 1D-layered models; (c,d) 3D models extracted from CVM-SI4.26. The color version of this figure is available only in the electronic edition.

average value as a function of azimuth (see Fig. 7); more attenuation tends to reduce ground-motion levels to a more average level at a particular R_{rup}. The variability at these short periods tends to be larger than the relations derived from observations, due to the large variation in ground motion in azimuthal regions parallel and perpendicular to the strike of the fault. This is likely due to coherent waves from directivity present in the 1D-layered model, later shown to be significantly reduced in more complex media.

Media Heterogeneity

In this section, we explore the effects on the synthetics from small- and broader-scale variation in the velocity and density model. In addition to the response from a 1D-layered model (often used in the absence of an accurate 3D-structure model or as representative of an average of path effects across a multitude of source azimuths, such as a GMPE database, Fig. 8), we discuss results from simulations using a 3D background CVM along an 80-km section of the San Andreas fault (Fig. 9) by plotting SA and within-event standard deviation in the same format as Figure 6. As hinted in the analysis of the effects of anelastic attenuation on ground motion shown above, the variation in parameters studied throughout the remainder of the article causes little difference in ground motions at long periods for the distance range investigated here; we thus choose to simplify the remaining figures by only including plots of metrics that are sensitive to frequencies above 1 Hz. We continue to group stations solely as a function of distance, with each station's corresponding GMPE predictions computed from the local values of $Z_{1.0}$, $Z_{2.5}$, and V_{S30} used in the simulation. We use anelastic models with power-law exponents of 0.6–0.8, deemed the most appropriate from the distance decay observed in the Anelastic Attenuation section. The simulations are compared to GMPE relations, including the variation in V_{S30} and depths to 1 and 2.5 km/s isosurfaces of V_S. We will use σ throughout this section to refer to the standard deviation used in models with small-scale heterogeneities.

As discussed in the Anelastic Attenuation section, Figure 7 shows that simulations in a 1D-layered media without small-scale heterogeneities have larger SAs within cone-shaped areas off the ends of the fault, compared to those along the fault, due to directivity effects persisting at the shorter periods. As frequency and distance from the source increase, scattering in the propagation media gradually weakens the directivity signature in models including small-scale heterogeneity. The directivity effects are further reduced (almost eliminated) at higher frequencies in models that include large-scale velocity variations (e.g., Fig. 7c,d, which plots GMRotD50 at $T = 0.3$ s) that serve to spatially redistribute the energy as a function of azimuth from the fault plane;

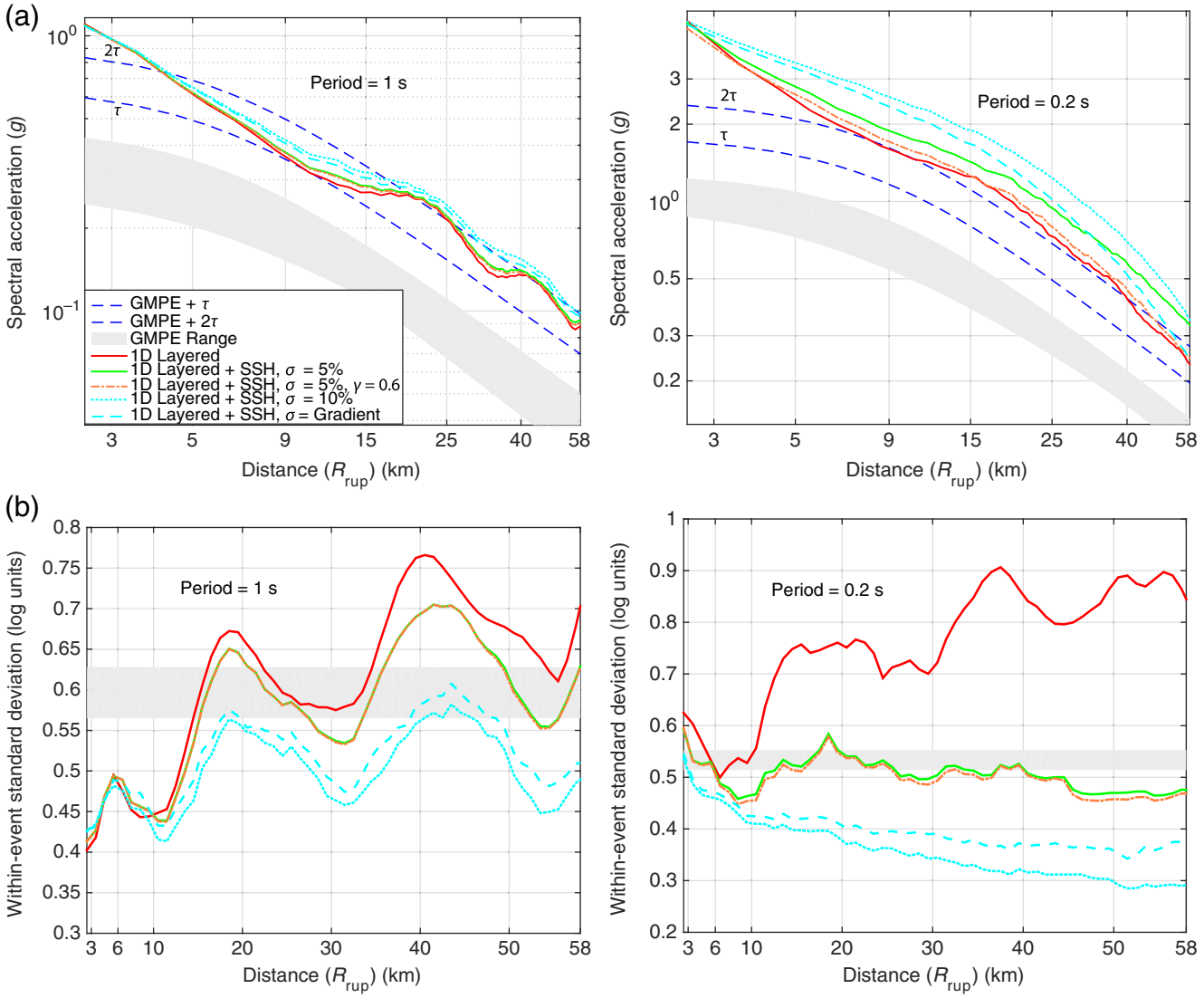

Figure 8. (a) SA and (b) intraevent variability for a characteristic long and short period showing the influence of several models of small-scale heterogeneity compared with GMPE predictions using a 1D-layered background velocity model. SSH, small-scale heterogeneity with a correlation length of 150 m. The color version of this figure is available only in the electronic edition.

the energy is not coherently directed outward from the hypocenter but is redistributed and scattered at depth before reaching the surface. These features agree with Somerville *et al.* (1997), who reported that directivity effects from large events are erased at short periods and found that a transition region of 1–4 Hz exists between where directivity and scattered wave energy dominates. The Ⓔ electronic supplement to this article plots histograms and q–q plots comparing the lognormality of residuals of 1D-layered and 3D background velocity models, showing that the distribution becomes more normally distributed when including more complexity in the media, a feature commonly observed in data sets of recorded ground motions.

The 1D-layered models (Fig. 8) that include statistically described media heterogeneity (constant σ of 5% and 10% and a gradient model) tend to increase the SAs, with stronger effects as frequencies increase. The gradient model ($\sigma = 10\%$ near the surface, linearly decreasing down to 2% at 7.5 km depth, and set to 2% below this), simulating the increase of normal stress as a function of depth with lithostatic pressure, produces SAs similar to those from the $\sigma = 10\%$ case near the source and approaches that from models with no heterogeneity ($\sigma = 0\%$) farther away. The largest effect on the ground-motion variability comes from models including small-scale heterogeneity that serves to reduce the variation as a function of azimuth at higher frequencies. A σ of 5% in small-scale heterogeneity leads to a fairly constant ground-motion variability as a function of distance, close to that from empirical estimates at higher frequencies (which, due to data limitations, typically employ a distance-independent model). The models of small-scale heterogeneities with $\sigma = 10\%$ (including the gradient model) tend to generate variability lower than that of the GMPEs. The

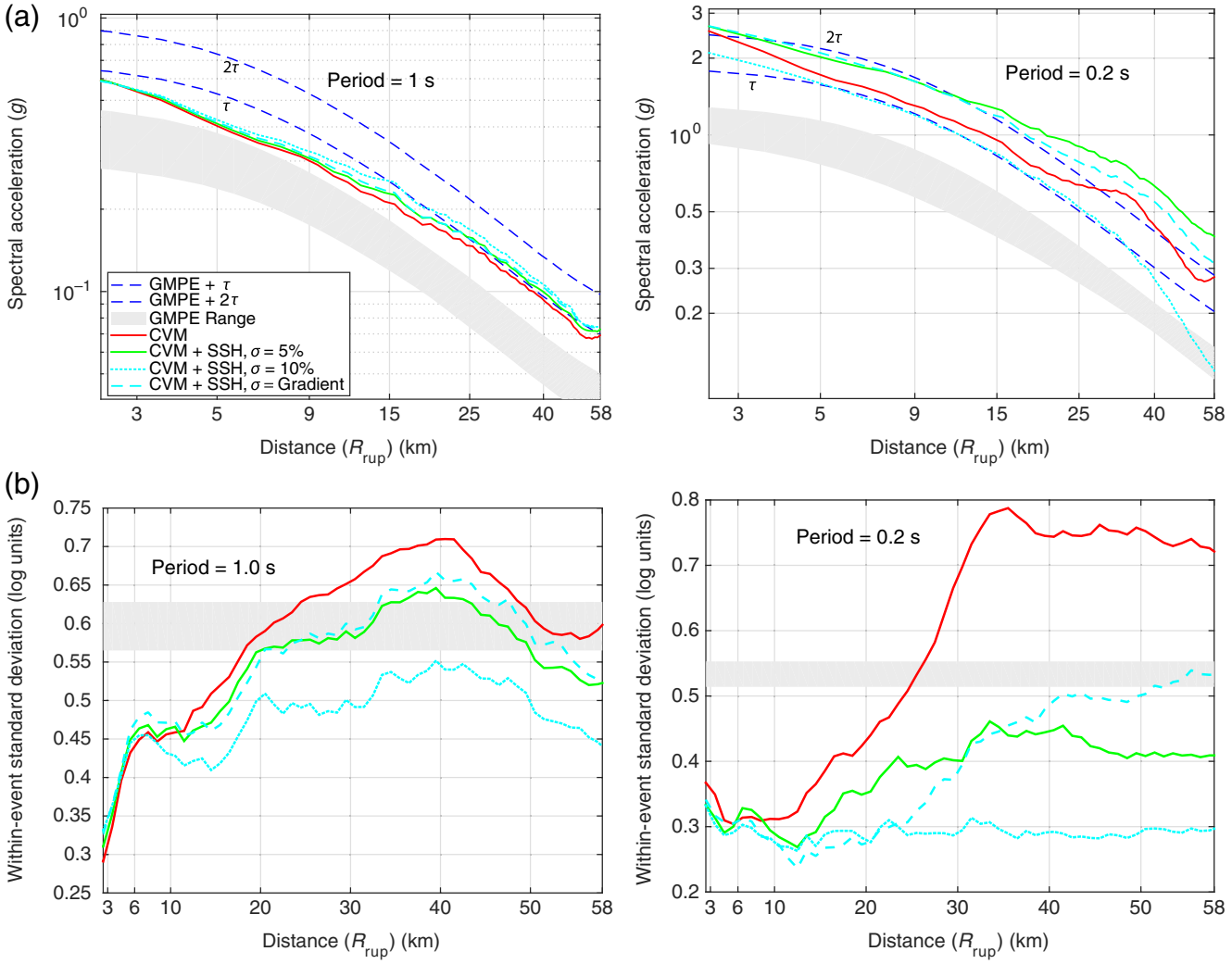

Figure 9. Similar to Figure 8. (a) SA and (b) intraevent variability using a 3D background model extracted from the CVM-SI4.26. The color version of this figure is available only in the electronic edition.

long-wavelength oscillations in the SAs and associated variability are likely scenario-specific source- and velocity-model effects, expected to average out for ensembles of multiple-source realizations.

Because of the reduction in broadband directivity from scattering that occurs at long wavelengths from the 3D background structure, SAs are significantly reduced at all distances from the fault, across all frequencies (compare Fig. 9 with Fig. 8). Moreover, the sharp parallel velocity discontinuities in the near surface present in the 1D-layered models, absent in the CVM, are likely causing amplified reverberations. The peak in the SAs near 40 km (most prominent at a period of 0.2 s) is likely related to the basin structure (see Fig. 4).

σ causes a significant change in SA values at high frequencies using a CVM superimposed with small-scale heterogeneities (Fig. 9). At 5% σ, we find similar results as in Figure 8 for 1D-layered models—the SA is increased. At 10% σ, however, we see that the SAs are reduced, particularly at larger distances from the source. The gradient σ model produces SAs that are increased compared to $\sigma = 0\%$ but lower than the 5% σ model at larger distances. Similar findings are obtained from the accelerograms for models in Figures 10 and 11 (extracted along a profile perpendicular to the fault) for 1D-layered and CVM background models, respectively, with distributions of small-scale heterogeneities with 0%, 5%, and 10% σ. We attribute this reduction in SAs for models with larger (near-surface) σ to a larger amount of downward scattered waves that attenuate within the upper mantle (the deepest portion of our model), facilitated by the smoother 3D velocity structure. This is in agreement with Korn (1993) who found that coda decay is dominated by the leaking of scattered energy into the mantle and not by inelastic effects (diffusion energy). The reason that previous simulation studies (e.g., Frankel and Clayton, 1986; Bydlon and Dunham, 2015) found that the σ of the small-scale heterogeneities scales the energy level in the coda may be related to their 2D model approximations as well as complexity in the background velocity models.

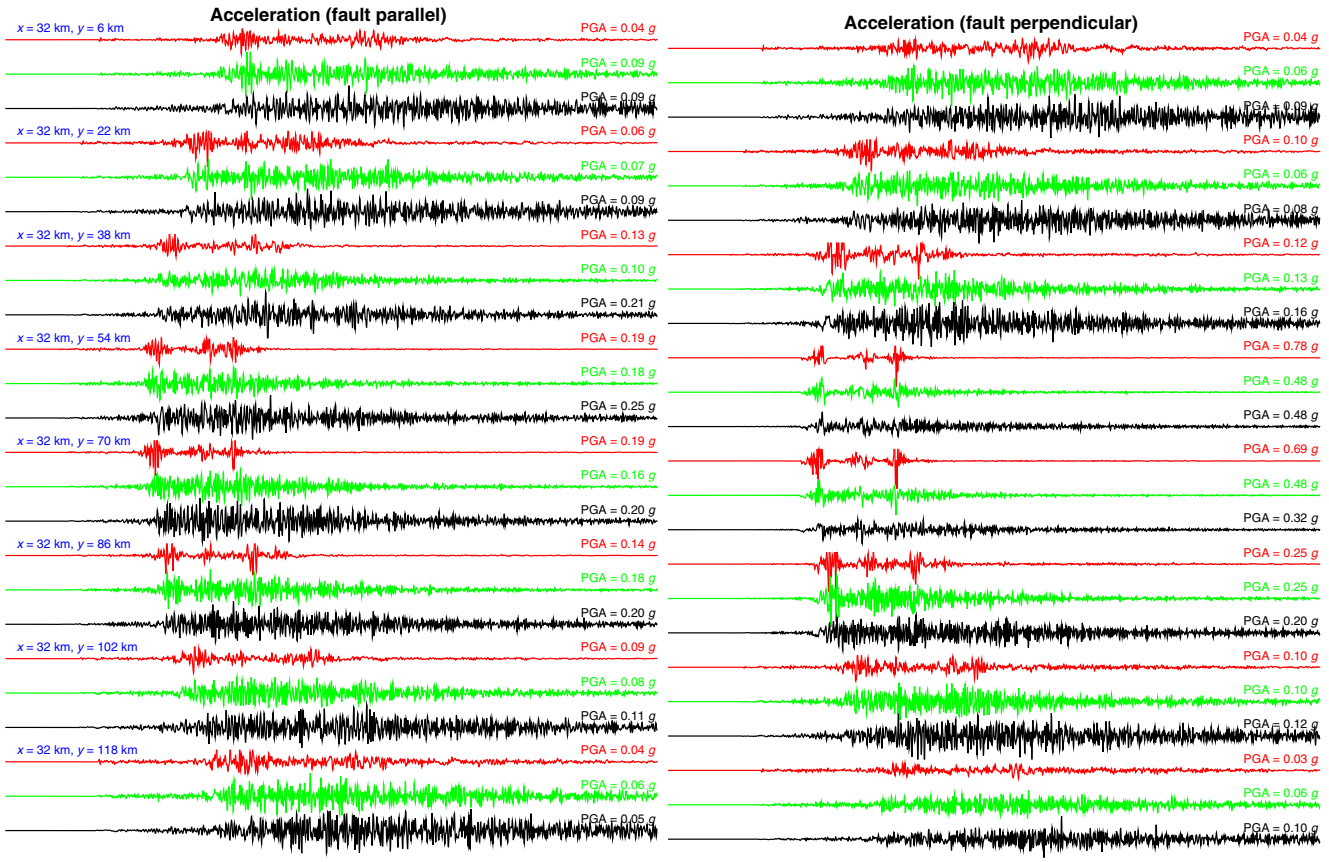

Figure 10. Acceleration time series extracted from the 1D-layered model profile perpendicular to the strike of the fault with 0, 5, and 10% σ in small-scale heterogeneity. Coordinate locations refer to model geometry in Figure 7. The color version of this figure is available only in the electronic edition.

Our simulations reveal a trade-off between the effects of scattering and intrinsic attenuation on ground motion. Figure 8 shows that a power-law Q model with an exponent of 0.6 with a σ of 5% small-scale heterogeneity reduces the SA 0.2 s to near the level of the model without small-scale heterogeneities but with a power-law exponent of 0.8. This trade-off is expected, because the smaller Q obtained at higher frequencies from $\gamma = 0.6$ counteracts the increased scattering from the models with 5% σ of the small-scale heterogeneities. On the other hand, the variation in γ is seen to have a negligible effect on the ground-motion variability (Fig. 8). The 5% σ model for both 1D-layered and CVM background velocity models shows the characteristic loss of energy from the main arrivals, due to scattering, and the increase in coda energy. This causes a significantly increased duration of energy, particularly at distances farther from the source. This is seen to both increase and decrease PGA, depending on site location. At higher σ in the CVM background model, we still see the same features as compared to the model without small-scale heterogeneity but with a significantly reduced coda amplitude. One explanation is that scattering disperses the energy over a longer time (reducing the peak oscillator response), but here, because the source itself already has a long duration, this added spreading of the energy has a relatively small effect. We hypothesize that a point source would have more typical effects, that is, scattering causing mainly attenuation because of the lack of directivity from the source.

Duration

Metrics that incorporate amplitude, frequency content, and duration of the ground motion across a broad frequency bandwidth are likely to be more reliable predictors of damage than ones only relating to ground-motion amplitude (e.g., PGA). Arias intensity (I_A) is a scalar parameter that captures the potential destructiveness of an earthquake as the integral of the acceleration time history, defined as $I_A = \pi/(2g) \int_0^{t_{max}} a(t)^2 dt$, in which $a(t)$ is the amplitude of the acceleration at time t, g is the acceleration due to gravity, and t_{max} is the total duration of the time series. Afshari and Stewart (2016) used the NGA-West2 data set to constuct a model for the duration dependence of 5%–95% normalized I_A, D_{5-95}, building off of previous work (Kempton *et al.*, 2006; Bommer *et al.*, 2009). Afshari and Stewart (2016) used additive path terms in their model with distance breaks at 10 and 50 km, in addition to a site term that increases duration for decreasing V_{S30} and larger basin depth.

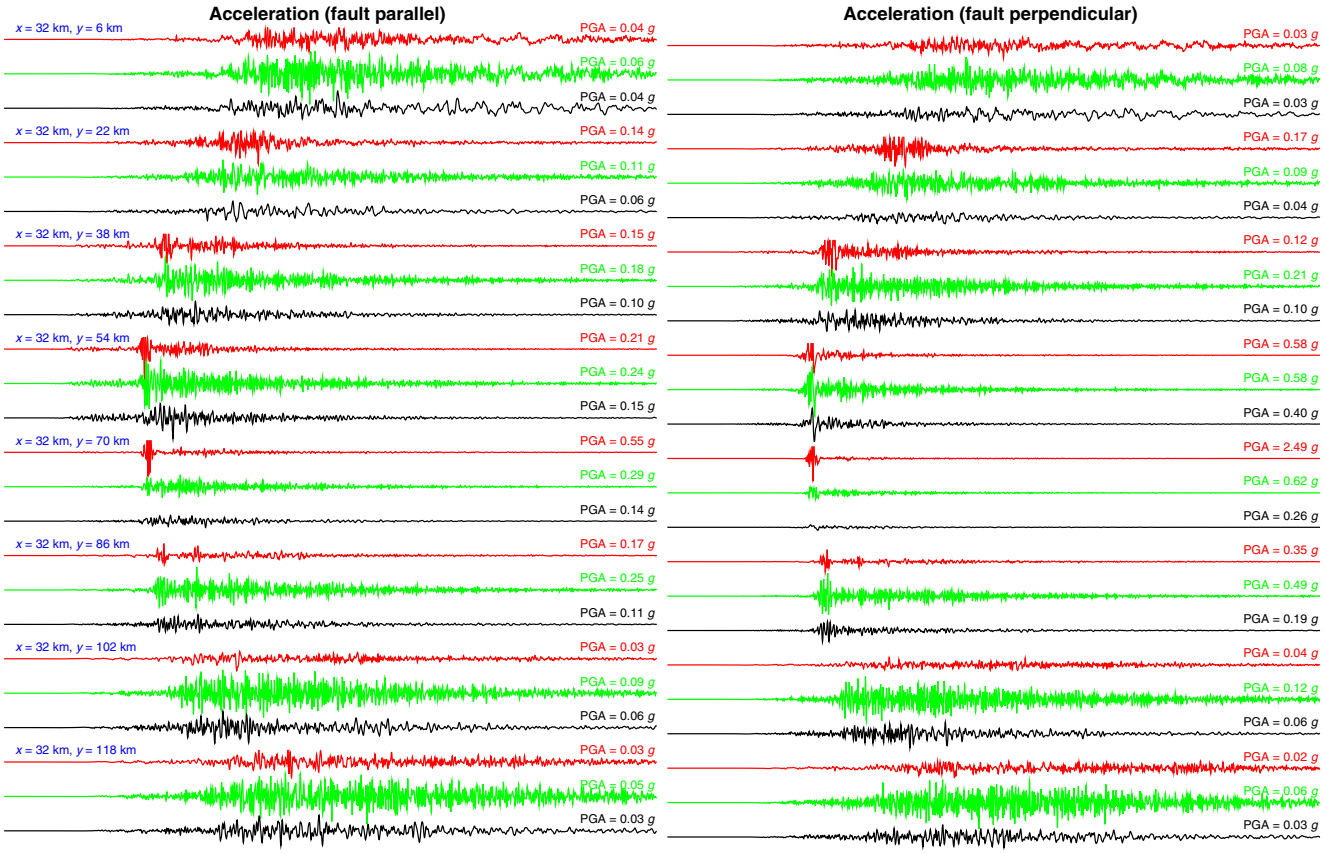

Figure 11. Similar to Figure 10 but using the background CVM. The color version of this figure is available only in the electronic edition.

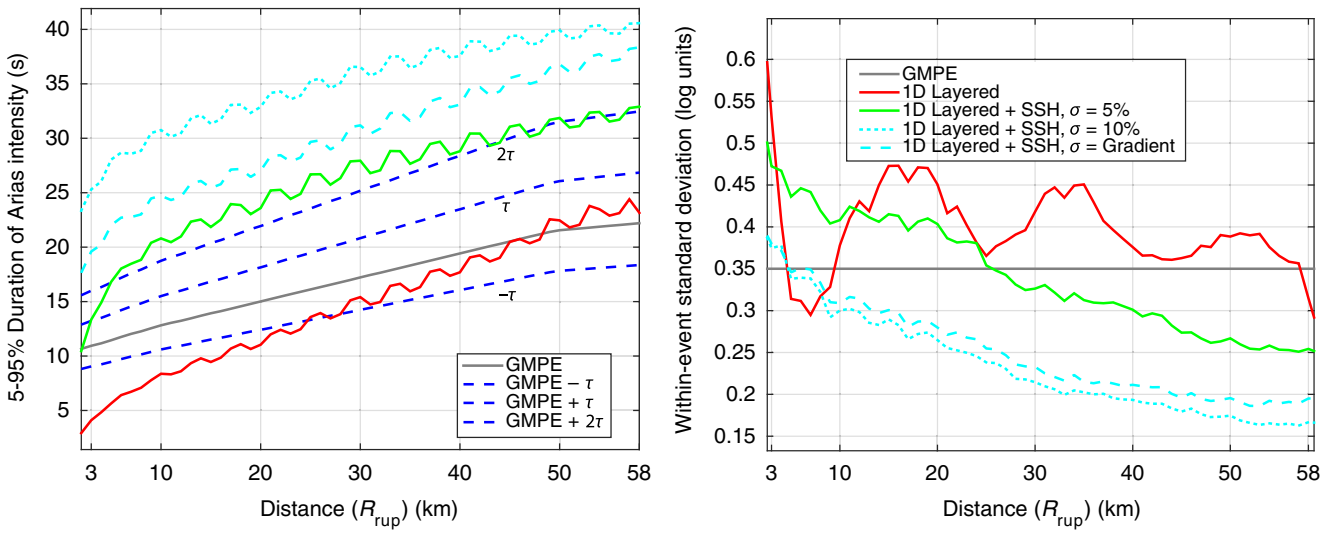

Figure 12. Median and intraevent variability for 5%–95% duration of Arias intensity for a 1D-layered structure. The color version of this figure is available only in the electronic edition.

Figures 12 and 13 plot the median and intraevent standard deviation of the 5%–95% duration of I_A for 1D-layered and CVM background models, respectively, compared with the Afshari and Stewart (2016) model. The horizontal components are used to compute the geometric mean of the synthetic ground motion, in which we focus on models with power-law $Q(f)$ exponents of 0.8 (with additional models plotted in Ⓔ Figs. S15 and S16). The complex source model combined with long-wavelength scattering from the 1D-layered structure produces a duration of a below-average

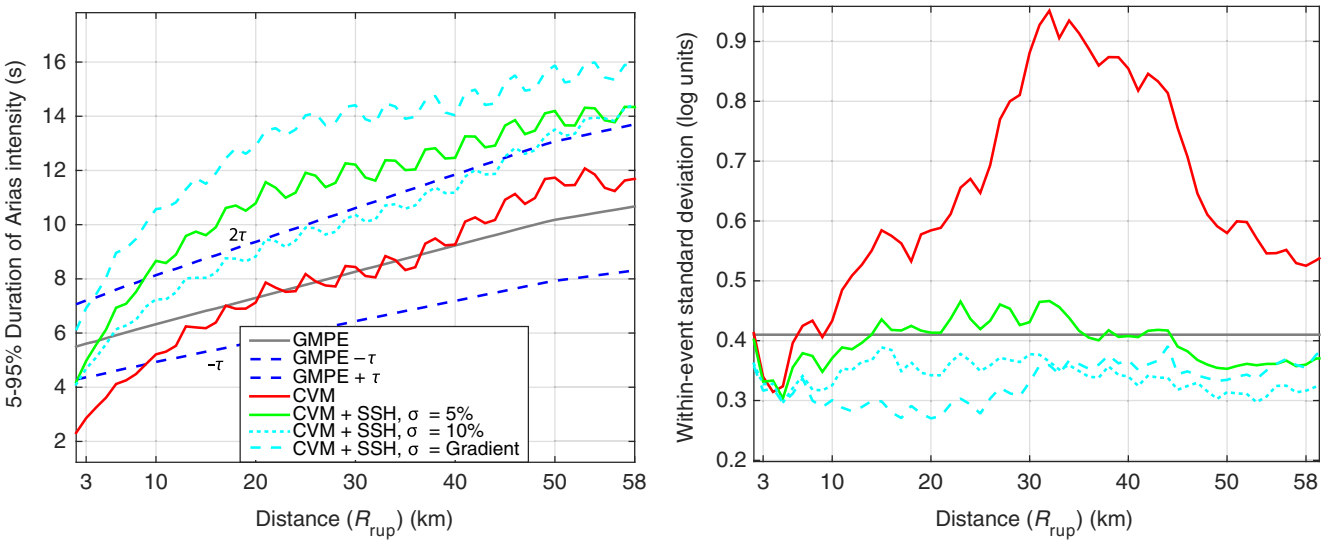

Figure 13. Similar to Figure 12 but using a 3D background model extracted from the CVM. The color version of this figure is available only in the electronic edition.

event at small R_{rup} but progressively increases as a function of distance. The addition of small-scale heterogeneity onto the background 1D-layered structure increases the 5%–95% duration significantly, near the level of the median plus two interevent standard deviations beyond ~5 km, using a 5% σ model of small-scale heterogeneity, and above that for larger σ models. We find, similar to that found from the analysis of SAs at shorter periods, the standard deviation tends to decrease (compared to models without small-scale heterogeneity) for models run in a small-scale heterogeneous structure. This may be (in part) because I_A is an acceleration based parameter, and thus is less sensitive to long periods in which rupture directivity is the strongest.

Similar characteristics to the 1D-layered results are present in simulations incorporating a background 3D model (shown in Fig. 13); the addition of small-scale heterogeneity produces the synthetic median 5%–95% duration trend with distance, similar to that of the GMPE. As in the case of high-frequency SA, there is a decrease in I_A at large σ (as well as for a longer correlation length plotted in Fig. S15). This is due to the reduced energy seen in the coda with higher σ, as seen in Figure 11. Models that include small-scale heterogeneity hover near the expected range of variability (with a large reduction compared to the model without small-scale heterogeneity), with larger σ-values corresponding to slightly smaller intraevent standard deviations.

Pulse Period

Strong velocity pulses caused by constructive interference of seismic waves as a rupture propagates along a fault are expected to occur far from the epicenter but close to the fault, amplifying the response at long periods. However, there are few records available in which directivity is most likely to occur. Given these data limitations, simulations may be able to provide a more accurate characterization of directivity pulses and near-fault ground motions than can observations alone. Here, we use the wavelet-analysis technique to isolate directivity effects by extracting the largest velocity pulse from the fault-normal ground motion (Baker, 2007). The pulse is only extracted if it has a large peak velocity and a high pulse indicator (defined by Baker, 2007, as a time-series metric that is effective in discriminating well-developed directivity pulses) greater than 0.85 that limits pulses to be early in the time history, when directivity pulses are more likely to occur. Additionally, the width of the pulses were assumed to be greater than 1 s, because directivity is primarily considered to exist most prominently at low frequencies for large-magnitude events.

Figure 14 plots the pulse period extracted from the fault-normal-component records for simulations with 1D-layered and CVM background models. Small-scale heterogeneity and frequency-dependent attenuation (for which in this study we set the transition frequency for Q at 1 Hz) have little effect on this metric, because it is primarily influenced by low frequencies. Pulses exist in regions near the fault rupture, extending out from the hypocenter, as expected from empirical observations. Interestingly, there are few pulses present off the ends of the fault in the 1D-layered simulation, in which directivity would be expected to be quite large from the spatial ground-motion map in Figure 7 (which plots SA at 3.3 Hz but is similar to the ground-motion pattern at lower frequencies). Additional simulations are needed to better quantify if this feature is consistent or related to the simplified velocity structure. The CVM background model introduces a lobe of directivity on the left end of the fault, with fairly short periods, that decreases in period with distance from the fault. This may be related to the velocity structure at depth, becauase Figure 4 shows that relatively high velocities exist in this region.

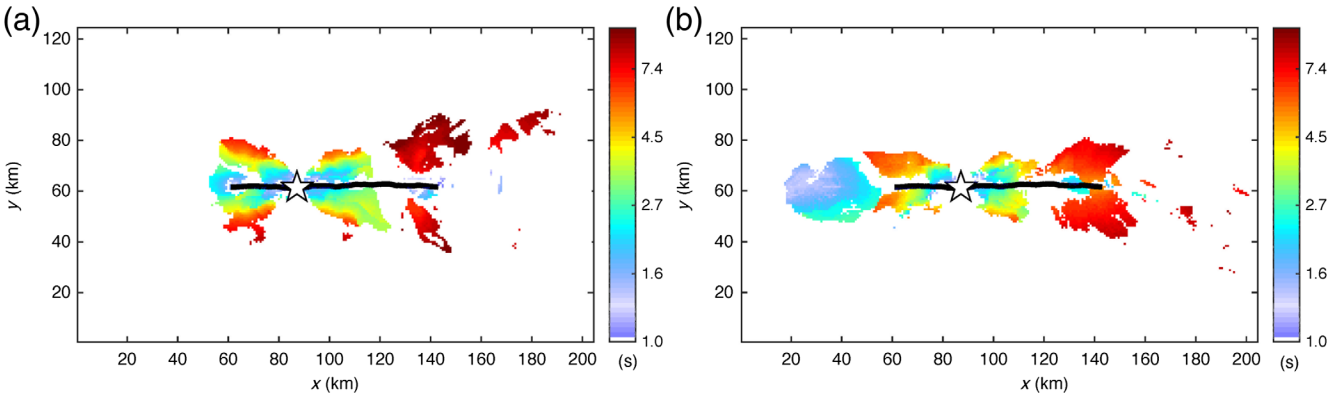

Figure 14. Regions where a directivity pulse occurs and its corresponding pulse period (s) for (a) 1D-layered and (b) 3D models. The color version of this figure is available only in the electronic edition.

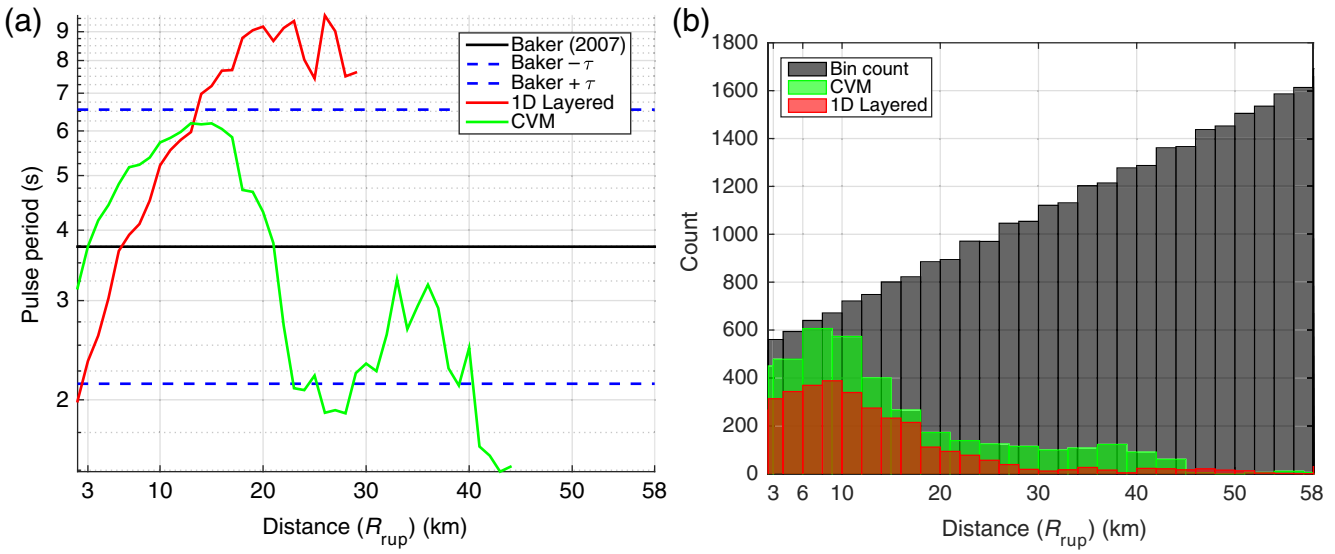

Figure 15. (a) Pulse period as a function of distance for results shown in Figure 14. (b) The number of stations at each distance, along with the number of stations observed to have a pulse period in 1D-layered and 3D models. The color version of this figure is available only in the electronic edition.

The pulse period is binned similarly to the SA analysis and plotted as a function of distance in Figure 15, along with the predictive relationship (Baker, 2007). It is seen that the CVM background structure reduces the pulse period above ~12 km R_{rup}, nearer to that of Baker (2007). Few stations have a pulse period beyond 30 km, as demonstrated in the histogram in Figure 15, agreeing with observations.

κ (Kappa)

Synthetic ground-motion records need to have a similar spectral decay to that of observations to be realistic at high frequencies. Anderson and Hough (1984) first described this spectral decay as κ by modeling it as an exponential decay, measured from above the corner frequency f_c up to the noise level or Nyquist frequency. They found consistent values for southern California records in the $\kappa = 0.04$–0.06 s range for hard-rock sites.

After band-pass filtering our seismograms to the resolution of the finite-difference grid (< 7.5 Hz and constrained by the total simulation time), we calculate κ from a linear least-squares fit to spectra across a defined bandwidth in frequency/log-amplitude space (taking the average of the two horizontal components). At individual stations, site amplification and source directivity effects introduce peaks in the spectra, making it difficult to accurately pick the slope. Thus, we stacked Fourier spectra as a function of R_{rup} to average out individual site response and reduce high-frequency oscillations; see Figure 16, for both 1D-layered and 3D models. We initially chose a narrow bandwidth (5–7 Hz) near where the Fourier acceleration energy in the majority of records starts to noticeably deviate from a flat spectrum. Using an attenuation relationship with a power-law exponent of

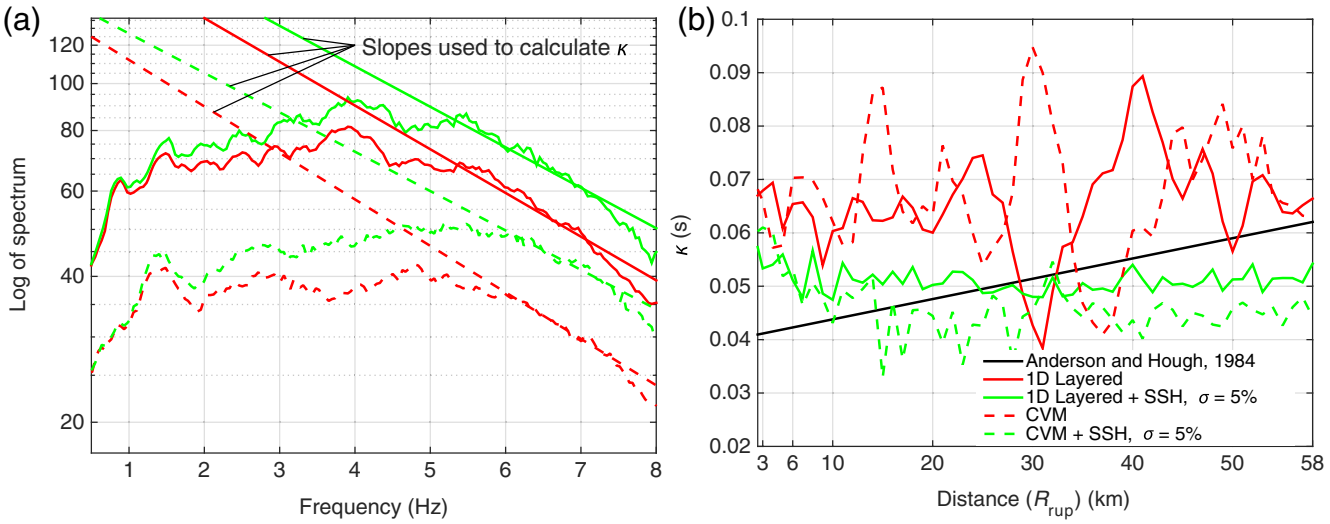

Figure 16. κ calculated for both 1D-layered and 3D models, with and without small-scale heterogeneity, using the relatively narrow bandwidth 5–7 Hz. (a) Example of calculating κ (from slopes of spectral amplitudes) using stacked energy at $R_{rup} = 5$ km. (b) κ compared with the Anderson and Hough (1984) empirical relation for hard-rock sites. SSH refers to small-scale heterogeneity (using the same choice of parameters specified in Fig. 3). All models use a $Q(f)$ exponent of 0.8. The color version of this figure is available only in the electronic edition.

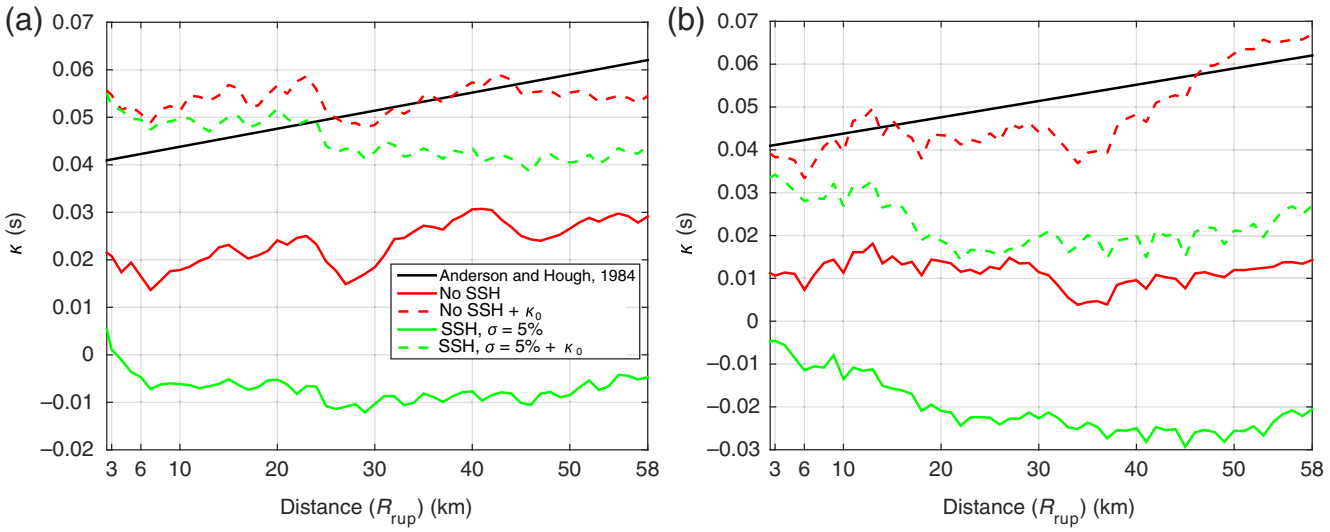

Figure 17. κ-values calculated over the bandwidth 2–7 Hz, using a constant-Q-layered model within the near surface to simulate κ_0 for (a) 1D-layered and (b) 3D models. SSH refers to small-scale heterogeneity (using the same choice of parameters specified in Fig. 3). All models use a $Q(f)$ exponent of 0.8. The color version of this figure is available only in the electronic edition.

$\gamma = 0.8$ and $Q_0 = 0.05 \times V_S$ (V_S in m/s) produces roughly similar values of κ to that found in Anderson and Hough (1984). Small-scale heterogeneity increases energy at high frequencies (> 1 Hz), reducing the slope in the spectra and thus decreasing the measured κ. This is in contrast to the observed increase in κ when including small-scale heterogeneity from site attenuation (stratigraphic filtering) as seen in Ktenidou *et al.* (2015). An increase in κ with distance is not observed, as seen in Anderson and Hough (1984). This may be due to the complicated influence of laterally propagating waves (e.g., surface waves), as well as 3D heterogeneity changing the ray paths to form multiples. We note that we varied the window length used to compute the spectra and found that it has little influence on the determination of κ, as long as the strong, energetic part of S waves is encapsulated (with deviations on the order of a few percent).

Next, instead of picking the frequency above which the spectra start to decrease linearly (f_E), Figure 17 plots κ from 2 to 7 Hz for both the 1D-layered and 3D models. κ is much smaller, even negative (in the model with small-scale hetero-

geneity), compared to fitting the spectrum across a narrow bandwidth. There are three main components that contribute to κ: the source, path, and site effect. Because the source's spectrum is approximately flat up to 8 Hz, we know that it should contribute negligibly to κ (on average). We hypothesize that because we have previously demonstrated that a $Q(f)$ model with a power-law exponent near 0.6–0.8 matches the decay in the energy of GMPE relations as a function of distance, the path effect is accurately modeled in our simulations. The site effect, known as κ_0, contributes to κ regardless of distance. Hough *et al.* (1988) hypothesized that a shallow attenuation layer exists along the near surface, overlying a less attenuating medium, and Abercrombie (1997) conjectured that 90% of total seismic attenuation in bedrock occurs in the upper 3 km of the Earth's crust. Recently, Houtte *et al.* (2011) also found that the superficial layers of the soil predominantly influence κ_0 but that there remains a component with a deeper origin as well.

Assuming that κ_0 corresponds to attenuation that S waves encounter when traveling up vertically through the geologic structure beneath the station, it is possible to estimate the contribution from the site effect in our current simulations by equating $\exp(-\pi f \kappa_0)$ and $\exp(\frac{-\pi f R}{V_S Q(f)})$, providing the relation $\kappa_0 = \frac{R}{V_S Q_S}$, in which R is distance, Q_S is the attenuation of shear waves, and V_S is the shear-wave velocity in that layer. Summing up the contributions in the top 3 km (assuming no scattering) and using Q_S from a constant-Q model (at the level of Q at 5 Hz in our power-law model), κ_0 is an order of magnitude smaller than the expected value (near 0.04 s) for western North America. Motivated by this result, we introduce a frequency-independent attenuation zone at the near-surface region (3 km) to simulate κ_0 (this assumes that κ_0 is primarily site attenuation from local geological conditions beneath the site, as suggested in Anderson and Hough, 1984). We use the relation $Q_S = 0.025 \times V_S$ to obtain a κ_0 value of ~0.03 for both the 1D-layered and 3D velocity models. The Q-values (15–50) are similar to those observed for class B V_{S30} values in the shallow crust (Assimaki *et al.*, 2008). This constant-Q layer in the near surface should have a nearly common attenuating effect at all stations. Thus, the shallow region introduces a site effect on κ, whereas the path effect is derived from the underlying region of $Q(f)$, with path attenuation arising from the much larger quality factor in the deeper crust. Figure 17 plots κ from simulations that include this κ_0 technique that is seen to bring κ estimated from the simulations into the range observed from seismic data.

Figure 18 plots SA median and intraevent variability (comparable to Fig. 9) for models with and without the shallow frequency-independent Q layer described above for a CVM background model (Fig. S17 shows the corresponding results for 1D-layered models). The κ_0 implementation reduces ground-motion medians (most pronounced at the higher frequencies) to near the range of the GMPE values, with a distance dependence similar to that observed in GMPE models. The intraevent variability is slightly increased in models that include the κ_0 approach. It is thus still necessary to include small-scale heterogeneity in our models to match the intraevent variability of GMPEs, bringing the variability to be near the range of GMPE models at distances greater than about 30 km (although we note that κ_0 reduces the variability at high frequencies in the 1D-layered simulation without small-scale heterogeneity to align near that of empirical observations, as shown in Fig. S17).

Discussion

One goal of generating realistic ground motion is to complement the strong-motion database, because recordings in the near field of large earthquakes are sparse. Additionally, extending deterministic ground-motion prediction to higher frequencies is invaluable for structural engineers to help better constrain seismic hazard in the bandwidth important for engineering applications, because information inferred from simulations may have a significant impact on seismic hazard estimation. Before these goals are achieved, validation of physics-based 3D ground-motion synthetics is needed to ensure the decay of energy at high frequencies in the source model and that the trend in ground motion as a function of distance is consistent with observations of empirical ground motion. In this work, we compared our deterministic ground motion with that of empirical observations that make up GMPEs, focusing on the median and intraevent variability. Some of the unanswered questions and possible ramifications observed in our simulations that may impact seismic hazard assessment are discussed below.

Median Ground Motion

The ground-motion distance attenuation is controlled by geometric spreading of the wavefield, anelastic attenuation, scattering effects, and body- to surface-wave conversion. The effect of both anelastic attention and scattering is to reduce amplitudes of the first propagation impulse, and scattering leads to the redistribution of seismic-wave energy, transferred from low frequencies in the main arrival to higher frequencies in arrivals later in the signal. Many studies looked at contributions from scattering and attenuation (e.g., Mayeda and Koyanagai, 1992) and the separation of the two (e.g., Fehler *et al.*, 1992). The total apparent attenuation (Q_{app}) comes from the combined effect of both intrinsic (Q_i) and scattering attenuation (Q_S): $\frac{1}{Q_{\text{app}}} = \frac{1}{Q_i} + \frac{1}{Q_S}$ (Parolai *et al.*, 2015).

We find a complex relationship between the amplitude of median ground motion and the level of σ in models including small-scale media heterogeneity, in which the behavior is dependent on the background velocity model. The full time-series metrics analyzed (SA and duration) generally increase in 1D-layered models regardless of σ, but in the CVM, with reduced directivity at high frequency, a change from $\sigma = 5\%$ to 10% reduces the peak ground motion: the σ parameter does not seem to directly control the scattering intensity

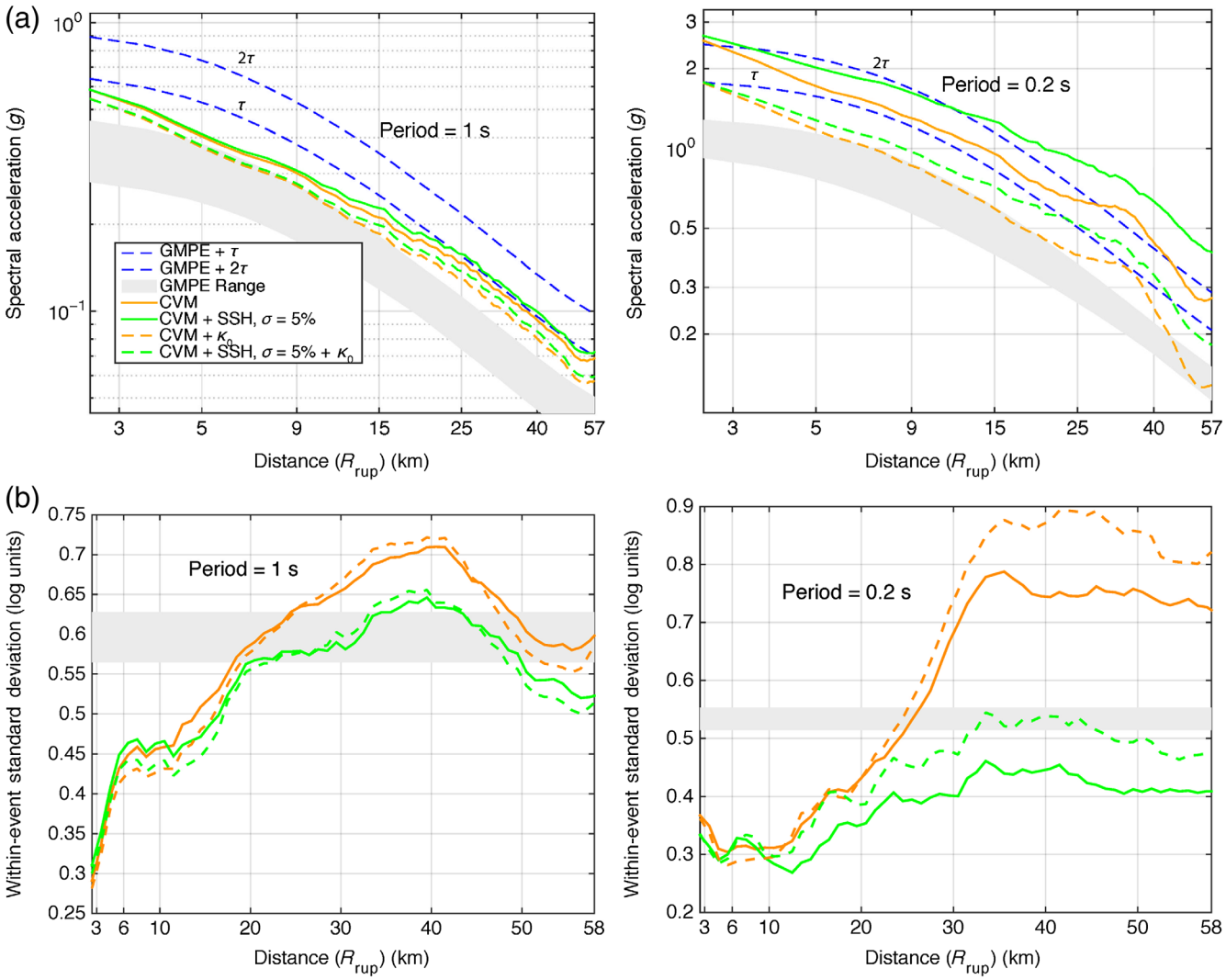

Figure 18. (a) SA at 1 and 0.2 s and (b) corresponding intraevent variability, using the 3D model with and without the κ_0 method. SSH refers to small-scale heterogeneity (using the same choice of parameters specified in Fig. 3). All models use a $Q(f)$ exponent of 0.8. The color version of this figure is available only in the electronic edition.

as a simple scaling factor. As evident from Figures 10 and 11, scattering disperses the energy over a longer time (reducing the peak oscillator response) but here, because the source itself already has a finite length and duration, this added spreading of the energy has a relatively small effect. More simulations are needed to fine-tune the relationship between source size and apparent attenuation and the combination of scattering and intrinsic effects in waveforms.

Even with the relatively high level of ground motion (above a median event), we find that we were able to validate characteristics of ground motion observed in the GMPEs, such as the distance decay at both short and long periods. It is likely that features such as this, related mainly to the path term, will remain true for a lower stress-drop event. We note that the median ground motion is larger here, as compared to Shi and Day (2013), for a few reasons (the moment magnitude M_w 7.12 in this article for a 1D-layered model is lower than that of Shi and Day, 2013, for a homogenous velocity model, mainly attributed to the lower shear modulus values, that serves to reduce the seismic moment). The most significant reason is likely that we include ground motion off the ends of the fault, where the largest ground motion occurs (as seen in Fig. 7), omitted by Shi and Day (2013) (as that spatial region was beyond the SORD simulations). Another possible reason for the increase is the 1D-layered velocity model serves to trap surface waves in a waveguide, compared to the homogeneous half-space used by Shi and Day (2013) (although the impedance is likely accounted for, because Shi and Day, 2013 used propagator matrices to correct ground motion to a western North America rock site). Finally, we exclude plasticity in the wave propagation (AWP) that may strongly damp ground motions near the fault (that would serve to reduce the ground motion), because the dynamic simulation already includes nonlinear effects from Drucker–Prager plasticity. As noted in Shi and Day (2013), inelastic strain deformation occurs near the free surface, induced by

stress waves from the dynamic rupture at depth. There, the extent of nonnegligible irreversible strain extends to fault-normal distances of up to 5–10 km from the fault. Shi and Day (2013) found that PGA measurements from simulations without plasticity in a homogenous medium are, on average, 50% larger than those from simulations with plasticity. It is likely that nonlinear effects would cause a reduction in peak ground motion (even at low frequencies, see Roten *et al.*, 2014) at similar distances from the fault and even further, as supported by the companion paper, in which reduced ground motion is seen beyond the regions of permanent plastic strain (Withers *et al.*, 2018).

The fault boundary condition approach of Roten *et al.* (2016) is needed to resolve the double counting of plasticity that is present if plasticity is included in the kinematic simulations. In the companion paper to this article (Withers *et al.*, 2018), we choose to neglect plastic effects in the dynamic simulation but include them in the kinematic step, which is shown to be important in regions of near-surface low shear-wave velocities. In this work, we found that excluding plasticity in the kinematic simulations had a negligible effect on the accuracy of the two-step approach, because most of the off-fault plastic strain occurs in the near surface, where the final slip is small (minimally affecting the moment magnitude).

Previous works (such as Lee *et al.*, 2008, 2009; Mai and Imperatori, 2015) have shown the importance of topographic scattering on near-field ground-motion simulations. This additional complexity is excluded in the simulations within this article, allowing a more general analysis with GMPEs. Future work should continue to investigate the trade-off between scattering from small-scale heterogeneities and surface topography, in combination with anelastic attenuation and its relation to median ground motion and variability.

Several tests were performed to ensure that the spatial selection of stations did not bias the results. Because of the regular grid of synthetic stations, the bins for small R_{rup} contain many more stations at azimuths near the fault strike (with reference to the hypocenter), compared with the fault-perpendicular direction. One test sorted stations into different-size bin widths, ranging from 1 to 20 km. The analysis produced similar results, albeit at a lower resolution for the wider bins. We analyzed for spatial bias by choosing a random selection of points within the medium and found negligible differences in binned ground motion. Additionally, assigning the same number of receivers in both the forward and backward directivity regions, as described in Somerville *et al.* (1997) and Spudich *et al.* (2013) (see Ⓔ the electronic supplement for a spatial map of the predicted directivity coefficient) produced no bias; the medians were indistinguishable.

To approximate the effects of omitting the lower near-surface velocities, we used adjustment factors from Boore *et al.* (2015) to correct the SAs in models with media heterogeneity from a reference value of V_{S30}. This had a negligible effect on the medians and variability, with the corrected trends lying almost identically on top of the unmodified ones. We chose not to consider the variation in $Z_{2.5}$ that would likely average out as well. Additionally, we note that there is no significant difference in the effects of varying the random seed used in generating the distributions of the small-scale heterogeneity (see Ⓔ Fig. S17). The method of binning a large number of stations together averages out any differences that may be seen from different small-scale media structure. However, if we chose to look at individual stations, a suite of random velocity models should be used to determine the range of SAs expected from variations in velocity structure. We also find that the correlation length has little effect on SA medians at a specific period (Ⓔ Fig. S17).

ϕ (Intraevent Variability)

The within-event residuals represent azimuthal variations in the source, path, and site effects that are not captured by a simple distance metric and a site classification based on the average shear-wave velocity. We find that stronger intrinsic attenuation (lower Q) can serve to decrease the intraevent standard deviation, as a result of the reduction in the amplitudes of seismic waves. Small-scale heterogeneity also significantly reduces the intraevent variability to (generally) better agree with GMPEs, being more pronounced at distances corresponding to a larger number of wavelengths from the source. This suggests the need for a highly complex velocity model to fit ground-motion variability, at least when considering a bilateral strike-slip event.

Atkinson (2006) found that variability for individual stations (ϕ_{ss}, known as the event-corrected single-station standard deviation or single-station ϕ) is less than that of the overall variability and was reduced even further when observations were restricted to a fixed azimuth range from a single fault (single-path standard deviation). Lin *et al.* (2011) found that single-site standard deviations are about 10% smaller than the total standard deviation, whereas the single-path standard deviation is about 50% smaller. Rodriguez-Marek *et al.* (2013) found that ϕ_{ss} is largely region independent, with an average value of $\phi_{ss} = 0.45$ fitting the data across all periods, with little variation with V_{S30}. We propose that the intraevent standard deviation in our 1D-layered model may be lower than expected from the ergodic assumption because we have no site effects, and at large distances from the source, path effects are minimal. Variability is overshadowed by directivity effects in our simulations but is lower than observations when small-scale heterogeneity is included, with 5% σ and even smaller strength in the gradient model and 10% σ at short periods.

Several previous studies used simulations to focus on specific aspects of variability, typically confined to low-frequency and/or simple velocity models (Vyas *et al.*, 2016; Crempien and Archuleta, 2017). For example, Imtiaz *et al.* (2015) found that the variability for bilateral strike-slip faults tends to increase with distances up to about 20 km for PGV (up to 3 Hz) and above this increases more gradually from

the source. This distance trend agrees with our simulations, in which at long periods (where intraevent variability is likely controlled by source parameters), ϕ increases rapidly up to about 20 km, with a more moderate increase above this, up to the maximum distance considered here (60 km). This systematic path effect variability should be studied more in the future, to determine if it is possible to better characterize uncertainty in ground-motion prediction.

Conclusions

Whereas previous deterministic ground-motion studies have been limited by available computational resources, here we have used the GPU capabilities of the Titan supercomputer to extend ground-motion prediction to higher frequencies using a fourth-order staggered-grid finite-difference method (AWP-ODC) with a 20 m grid implementing geometrical fault complexity. Specifically, the slip rates (with an omega-squared spectrum) from a dynamic simulation along a rough-fault topography are used as the input to our wave-propagation code. We include frequency-dependent attenuation via a power law above a reference frequency for both 1D-layered and CVM background models and superimpose small-scale heterogeneity in the entire domain using a range of statistical parameters. We quantify the contributions of small-scale fault geometric complexity and small-scale velocity and density inhomogeneities in the medium that can affect the ground-motion intensity and compared the synthetic ground motion with recent NGA relations. By binning stations as a function of distance, we compared several metrics with empirical predictions, including SA at varying periods and the duration of Arias intensity.

We find that for this particular rupture model, ground motion generally has a spectral decay that closely matches that of the GMPEs when using a power-law exponent between 0.6 and 0.8 above 1 Hz. We found that a 3D CVM extracted from southern California strongly affects the azimuthal distribution of radiated energy and rupture directivity by increasing the path complexity by long-wavelength scattering. We also investigated a proxy metric for directivity and found that characteristics from our simulations agree with observations; more events in varying media are needed to better determine the significance of hypocenter location and velocity model, but the results here are encouraging. Heterogeneity across all wavelengths is seen to consistently reduce the intraevent variability, due to the redistribution of energy as a function of azimuth at a specific distance. Long-period effects come mainly from long-wavelength features in the velocity model. Both short- and long-wavelength velocity perturbations affect the shorter periods, generally reducing them to values near that of observations. There is a trade-off between scattering and apparent attenuation with varying scale-length heterogeneous Earth structure.

Additionally, we examined the decay of high-frequency energy (κ) both as a function of frequency and distance, and find that our simulations have κ comparable to observations across a narrow bandwidth (5–7 Hz) but an order of magnitude smaller if using the entire high-frequency simulation bandwidth (2–7 Hz). We introduced a shallow near-surface frequency-independent low Q layer to modify the high-frequency energy decay that relates to κ. We showed that this approach has a significant effect at the high frequencies, while still retaining the appropriate distance relationship consistent with GMPEs. We observe that small-scale heterogeneity consistently reduces κ. As κ is primarily a high-frequency effect, having the most influence on spectral content for frequencies greater than 5–10 Hz, deterministic simulations that include even higher frequencies than studied here are needed to determine if this approach is necessary in the future.

Data and Resources

The southern California velocity model CVM-SI4.26 can be obtained from Southern California Earthquake Center (SCEC) at http://scec.usc.edu/scecpedia/. Most of the data-processing work was done using MATLAB (http://www.mathworks.com/products/matlab/). Figures were prepared using MATLAB and the Generic Mapping Tools package (http://www.soest.hawaii.edu/gmt/). All electronic addresses referenced here were last accessed on September 2016. All other data used in this article came from published sources listed in the references.

Acknowledgments

This research was supported through the Southern California Earthquake Center (SCEC) by the National Science Foundation (NSF) Cooperative Agreement EAR-0529922 and the U.S. Geological Survey (USGS) Cooperative Agreement 07HQAG0008, by USGS Award G15AP00077, and by NSF Awards EAR-1135455, OCI-114849, EAR-1349180, and ACI-1450451. The simulations were generated on the Titan Cray XK7 at the Oak Ridge Leadership Computing Facility in Tennessee. This is SCEC publication number 8068. The authors thank Associate Editor Adrian Rodriguez-Marek and reviewers Robert Graves and P. Martin Mai for comments contributing to an improved article. In addition, the authors are grateful to Brendon Bradley for helpful discussion and suggestions.

References

Abercrombie, R. E. (1997). Near-surface attenuation and site effects from comparison of surface and deep borehole recordings, *Bull. Seismol. Soc. Am.* **87,** 731–744.

Abrahamson, N. A., W. J. Silva, and R. Kamai (2014). Summary of the ASK14 ground motion relation for active crustal regions, *Earthq. Spectra* **30,** 1025–1055.

Afshari, K., and J. P. Stewart (2016). Physically parameterized prediction equations for significant duration in active crustal regions, *Earthq. Spectra* **22,** 985–1003.

Anderson, J., and S. Hough (1984). A model for the shape of the Fourier amplitude spectrum of acceleration at high frequencies, *Bull. Seismol. Soc. Am.* **74,** 1969–1993.

Andrews, J., and S. Ma (2016). Validating a dynamic earthquake model to produce realistic ground motion, *Bull. Seismol. Soc. Am.* **106,** 665–672.

Assimaki, D., W. Li, J. H. Steidl, and K. Tsuda (2008). Site amplification and attenuation via downhole array seismogram inversion: A compar-

ative study of the 2003 Miyagi-Oki aftershock sequence, *Bull. Seismol. Soc. Am.* **98,** 301–330.

Atik, L. A., N. Abrahamson, J. J. Bommer, F. Scherbaum, F. Cotton, and N. Kuehn (2010). The variability of ground-motion prediction models and its components, *Seismol. Res. Lett.* **81,** 794–801.

Atkinson, G. M. (2006). Single-station sigma, *Bull. Seismol. Soc. Am.* **96,** 446–455.

Baker, J. W. (2007). Quantitative classification of near-fault ground motions using wavelet analysis, *Bull. Seismol. Soc. Am.* **97,** 1486–1501.

Baumann, C., and L. A. Dalguer (2014). Evaluating the compatibility of dynamic rupture-based synthetic ground motion with empirical ground-motion prediction equation, *Bull. Seismol. Soc. Am.* **104,** 1–19.

Ben-Zion, Y., and C. Sammis (2003). Characterization of fault zones, *Pure Appl. Geophys.* **160,** 677–715.

Bielak, J., R. W. Graves, K. B. Olsen, R. Taborda, L. Ramirez-Guzman, S. M. Day, G. P. Ely, D. Roten, T. H. Jordan, P. J. Maechling, *et al.* (2010). The ShakeOut earthquake scenario: Verification of three simulation sets, *Geophys. J. Int.* **180,** 375–404.

Bommer, J. J., P. J. Stafford, and J. E. Alarcón (2009). Empirical equations for the prediction of the significant, bracketed, and uniform duration of earthquake ground motion, *Bull. Seismol. Soc. Am.* **99,** 3217–3233.

Boore, D. M. (2006). Orientation-independent measures of ground motion, *Bull. Seismol. Soc. Am.* **96,** 1502–1511.

Boore, D. M., J. P. Stewart, E. Seyhan, and G. Atkinson (2015). NGA-West 2 equations for predicting PGA, PGV, and 5%-damped PSA for shallow crustal earthquakes, *Earthq. Spectra* **30,** 1057–1085.

Bydlon, S. A., and E. M. Dunham (2015). Rupture dynamics and ground motions from earthquakes in 2-D heterogeneous media, *Geophys. Res. Lett.* **42,** 1701–1709.

Campbell, K., and Y. Bozorgnia (2014). NGA-West2 ground motion model for the average horizontal components of PGA, PGV, and 5%-damped linear acceleration response spectra, *Earthq. Spectra* **30,** 1087–1115.

Chiou, B. S. J., and R. R. Youngs (2014). Update of the Chiou and Youngs NGA model for the average horizontal component of peak ground motion and response spectra, *Earthq. Spectra* **30,** 1117–1153.

Crempien, J., and R. Archuleta (2017). Within-event and between-events ground motion variability from earthquake rupture scenarios, *Pure Appl. Geophys.* **174,** no. 9, 3451–3465.

Cui, Y., E. Poyraz, K. B. Olsen, J. Zhou, K. Withers, S. Callaghan, J. Larkin, C. Guest, D. Choi, A. Chourasia, *et al.* (2013). Physics-based seismic hazard analysis on petascale heterogeneous supercomputers, *Proc. of the International Conf. on High Performance Computing, Networking, Storage and Analysis*, Denver, Colorado, 17–22 November 2013.

Day, S. M., L. A. Dalguer, and N. Lapusta (2005). Comparison of finite difference and boundary integral solutions to three-dimensional spontaneous rupture, *J. Geophys. Res.* **110,** 1–23.

Day, S. M., R. Graves, J. Bielak, D. Dreger, S. Larsen, K. B. Olsen, A. Pitarka, and L. Ramirez-guzman (2008). Model for basin effects on long-period response spectra in southern California, *Earthq. Spectra* **24,** 257–277.

Dunham, E. M., D. Belanger, L. Cong, and J. E. Kozdon (2011). Earthquake ruptures with strongly rate-weakening friction and off-fault plasticity, part 2: Nonplanar faults, *Bull. Seismol. Soc. Am.* **101,** 2308–2322.

Ely, G. P., S. M. Day, and J.-B. Minster (2009). A support-operator method for 3-D rupture dynamics, *Geophys. J. Int.* **177,** 1140–1150.

Ely, G. P., T. H. Jordan, P. Small, and P. J. Maechling (2010). A V_{s30}-derived near surface seismic velocity model, *AGU Fall Meeting*, San Francisco, California, S51A-1907.

Fehler, M., M. Hoshiba, H. Sato, and K. Obara (1992). Separation of scattering and intrinsic attenuation for the Kanto-Tokai region, Japan, using measurements of S-wave energy versus hypocentral distance, *Geophys. J. Int.* **108,** 787–800.

Frankel, A., and R. W. Clayton (1986). Finite difference simulations of seismic scattering: Implications for the propagation of short-period seismic waves in the crust and models of crustal heterogeneity, *J. Geophys. Res.* **91,** 6465–6489.

Graves, R., and A. Pitarka (2010). Broadband ground-motion simulation using a hybrid approach, *Bull. Seismol. Soc. Am.* **100,** 2095–2123.

Graves, R., and A. Pitarka (2016). Kinematic ground motion simulations on rough faults including effects of 3D stochastic velocity perturbations, *Bull. Seismol. Soc. Am.* **106,** 2136–2153.

Graves, R., T. Jordan, S. Callaghan, E. Deelman, E. Field, G. Juve, C. Kesselman, P. Maechling, G. Mehta, K. Milner, *et al.* (2010). CyberShake: A physics-based seismic hazard model for southern California, *Pure Appl. Geophys.* **168,** 367–381.

Hartzell, S., M. Guatteri, P. M. Mai, P.-C. Liu, and M. Fisk (2005). Calculation of broadband time histories of ground motion, part II: Kinematic and dynamic modeling using theoretical Green's functions and comparison with the 1994 Northridge earthquake, *Bull. Seismol. Soc. Am.* **95,** 614–645.

Hartzell, S., S. Harmsen, and A. Frankel (2010). Effects of 3D random correlated velocity perturbations on predicted ground motions, *Bull. Seismol. Soc. Am.* **100,** 1415–1426.

Hough, S., J. Anderson, J. Brune, F. Vernon, J. Berger, J. Fletcher, L. Haar, T. Hanks, and L. Baker (1988). Attenuation near Anza California, *Bull. Seismol. Soc. Am.* **78,** 672–691.

Houtte, C. V., S. Drouet, and F. Cotton (2011). Analysis of the origins ofκ (kappa) to compute hard rock to rock adjustment factors for GMPEs, *Bull. Seismol. Soc. Am.* **101,** 2926–2941.

Huang, Y., J.-P. Ampuero, and D. Helmberger (2014). Earthquake ruptures modulated by waves in damaged fault zones, *J. Geophys. Res.* **119,** 3133–3154.

Imperatori, W., and P. M. Mai (2013). Broadband near-field ground motion simulations in 3D scattering media, *Geophys. J. Int.* **192,** 725–744.

Imtiaz, A., M. Causse, E. Chaljub, and F. Cotton (2015). Is ground-motion variability distance dependent? Insight from finite-source rupture simulations, *Bull. Seismol. Soc. Am.* **105,** 950–962.

Kempton, J. J., J. P. Stewart, and M. Eeri (2006). Prediction equations for significant duration of earthquake ground motions considering site and near-source effects, *Earthq. Eng. Struct. Dynam.* **22,** 985–1013.

Kohler, M. D., H. Magistrale, and R. W. Clayton (2003). Mantle heterogeneities and the SCEC reference three-dimensional seismic velocity model version 3, *Bull. Seismol. Soc. Am.* **93,** 757–774.

Korn, M. (1993). Determination of site-dependent scattering Q from P-wave coda analysis with an energy-flux model, *Geophys. J. Int.* **113,** 54–72.

Ktenidou, O.-J., N. A. Abrahamson, S. Drouet, and F. Cotton (2015). Understanding the physics of kappa (κ): Insights from a downhole array, *Geophys. J. Int.* **203,** 678–691.

Lee, E., and P. Chen (2014). Full-3-D tomography for crustal structure in southern California based on the scattering-integral and the adjoint-wavefield methods, *J. Geophys. Res.* **119,** 6421–6451.

Lee, S.-J., H.-W. Chen, Q. Liu, D. Komatitsch, and B.-S. Huang (2008). Three-dimensional simulations of seismic-wave propagation in the Taipei basin with realistic topography based upon the spectral-element method, *Bull. Seismol. Soc. Am.* **98,** 253–264.

Lee, S.-J., D. Komatitsch, B.-S. Huang, and J. Tromp (2009). Effects of topography on seismic-wave propagation: An example from northern Taiwan, *Bull. Seismol. Soc. Am.* **99,** 314–325.

Lin, P.-S., B. Chiou, N. Abrahamson, M. Walling, C. Lee, and C. Cheng (2011). Repeatable source, site, and path effects on the standard deviation for empirical ground-motion prediction models, *Bull. Seismol. Soc. Am.* **101,** 2281–2295.

Magistrale, H., S. Day, R. W. Clayton, and R. Graves (2000). The SCEC southern California reference three-dimensional seismic velocity model version 2, *Bull. Seismol. Soc. Am.* **90,** 65–76.

Mai, P. M., and W. Imperatori (2015). The role of topography and lateral velocity heterogeneities on near-source scattering and ground-motion variability, *Bull. Seismol. Soc. Am.* **202,** 2163–2181.

Mai, P. M., M. Galis, K. Thingbaijam, J. Vyas, and E. M. Dunham (2017). Accounting for fault roughness in pseudo-dynamic ground-motion simulations, *Pure Appl. Geophys.* **174,** 3419–3450.

Mai, P. M., W. Imperatori, and K. B. Olsen (2010). Hybrid broadband ground-motion simulations: Combining long-period deterministic synthetics with high-frequency multiple S-to-S backscattering, *Bull. Seismol. Soc. Am.* **100,** 2124–2142.

Mayeda, K., and S. Koyanagai (1992). A comparative study of scattering, intrinsic, and coda Q-1 for Hawaii, Long Valley, and central California between 1.5 and 15.0 Hz, *J. Geophys. Res.* **97,** 6643–6659.

Nakata, N., and G. C. Beroza (2015). Stochastic characterization of mesoscale seismic velocity heterogeneity in Long Beach, California, *Geophys. J. Int.* **203,** 2049–2054.

Olsen, K. B., S. M. Day, L. A. Dalguer, J. Mayhew, Y. Cui, J. Zhu, V. M. Cruz-Atienza, D. Roten, P. Maechling, T. H. Jordan, *et al.* (2009). ShakeOut-D: Ground motion estimates using an ensemble of large earthquakes on the southern San Andreas fault with spontaneous rupture propagation, *Geophys. Res. Lett.* **36,** L04303, doi: 10.1029/2008GL036832.

Parolai, S., D. Bindi, and M. Pilz (2015). κ_0: The role of intrinsic and scattering attenuation, *Bull. Seismol. Soc. Am.* **105,** 2–5.

Phillips, W. S., K. M. Mayeda, and L. Malagnini (2013). How to invert multi-band, regional phase amplitudes for 2-D attenuation and source parameters: Tests using the USArray, *Pure Appl. Geophys.* **171,** 469–484.

Power, W., and T. Tullis (1991). Euclidean and fractal models for the description of rock surface roughness, *J. Geophys. Res.* **96,** 415–424.

Raoof, M., R. Herrmann, and L. Malagnini (1999). Attenuation and excitation of three-component ground motion in southern California, *Bull. Seismol. Soc. Am.* **89,** 888–902.

Renard, F., C. Voisin, D. Marsan, and J. Schmittbuhl (2006). High resolution 3D laser scanner measurements of a strike-slip fault quantify its morphological anisotropy at all scales, *Geophys. Res. Lett.* **33,** L04305, doi: 10.1029/2005GL025038.

Ripperger, J., J. Ampuero, P. M. Mai, and D. Giardini (2007). Earthquake source characteristics from dynamic rupture with constrained stochastic fault stress, *J. Geophys. Res.* **112,** 1–17.

Rodriguez-Marek, A., F. Cotton, N. A. Abrahamson, S. Akkar, L. A. Atik, B. Edwards, G. A. Montalva, and H. M. Dawood (2013). A model for single-station standard deviation using data from various tectonic regions, *Bull. Seismol. Soc. Am.* **103,** 3149–3163.

Roten, D., Y. Cui, K. Olsen, K. Withers, W. Savran, P. Wang, and M. Dawei (2016). High-frequency nonlinear earthquake simulations on petascale heterogeneous supercomputers, *SC'16 Proc. of the International Conf. for High Performance Computing, Networking, Storage and Analysis*, Salt Lake City, Utah, 13–18 November, 1–14.

Roten, D., K. B. Olsen, S. M. Day, Y. Cui, and D. Fäh (2014). Expected seismic shaking in Los Angeles reduced by San Andreas fault zone plasticity, *Geophys. Res. Lett.* **41,** 2769–2777.

Roten, D., K. B. Olsen, J. C. Pechmann, and H. Magistrale (2011). 3D Simulations of M 7 earthquakes on the Wasatch fault, Utah, part I: Long-period (0–1 Hz) ground motion, *Bull. Seismol. Soc. Am.* **101,** 2045–2063.

Savran, W. H., and K. B. Olsen (2016). Model for small-scale crustal heterogeneity in Los Angeles basin based on inversion of sonic log data, *Geophys. J. Int.* **205,** 856–863.

Shaw, J. H., T. H. Jordan, and A. Pleasch (2014). Toward implementation of a stochastic description of fine scale basin velocity structure in the SCEC Community Velocity Model (CVM-H), *Technical Report, SCEC Report 14176*.

Shi, Z., and S. M. Day (2013). Rupture dynamics and ground motion from 3-D rough-fault simulations, *J. Geophys. Res.* **118,** 1122–1141.

Somerville, P. G., N. F. Smith, R. W. Graves, and N. A. Abrahamson (1997). Modification of empirical strong ground motion attenuation relations to include the amplitude and duration effects of rupture directivity, *Seismol. Res. Lett.* **68,** 199–222.

Spudich, P., J. Bayless, J. Baker, B. Chiou, B. Rowshandel, S. Shahi, and P. Somerville (2013). Final report of the NGA-West2 Directivity Working Group, *Technical Report, PEER*, 1–162.

Taborda, R., and J. Bielak (2014). Ground-motion simulation and validation of the 2008 Chino Hills, California, earthquake using different velocity models, *Bull. Seismol. Soc. Am.* **104,** 1876–1898.

Taborda, R., K. Olsen, R. Graves, F. Silva, N. Khoshnevis, W. Savran, D. Roten, Z. Shi, C. Goulet, J. Bielak, *et al.* (2016). Verification and validation of high-frequency ($f_{\max} = 5$ Hz) ground motion simulations of the 2014 M 5.1 La Habra, California, earthquake, *Proc. of the SCEC Annual Meeting*, Palm Springs, California, 11–14 September.

Takemura, S., T. Furumura, and T. Saito (2009). Distortion of the apparent S-wave radiation pattern in the high-frequency wavefield: Tottori-Ken Seibu, Japan, earthquake of 2000, *Geophys. J. Int.* **178,** 950–961.

Vyas, C., P. M. Mai, and M. Galis (2016). Distance and azimuthal dependence of ground-motion variability for unilateral strike-slip ruptures, *Bull. Seismol. Soc. Am.* **106,** 1584–1599.

Withers, K. B., K. B. Olsen, and S. M. Day (2015). Memory-efficient simulation of frequency-dependent Q, *Bull. Seismol. Soc. Am.* **105,** 3129–3142.

Withers, K. B., K. B. Olsen, S. M. Day, and Z. Shi (2018). Validation of deterministic broadband ground motion and variability from simulations of buried thrust earthquakes, *Bull. Seism. Soc. Am.* doi: 10.1785/0120180005.

Department of Geological Science
5500 Campanile Drive
San Diego State University
San Diego, California 92182
kwithers@usgs.gov
kbolsen@mail.sdsu.edu
sday@mail.sdsu.edu
zshi@mail.sdsu.edu

Manuscript received 8 January 2018;
Published Online 13 November 2018